Nomination form for the 2020 Nishina Asia Award No.21-8

Candidate (name, affiliation, curriculum vitae including the date of the degree of Ph.D., nationality, address, email and telephone)

Name
Chen Fang
Affiliation
Institute of Physics, Chinese Academy of Sciences
Contact
8 Zhongguancun South 3rd St., Beijing 100190, China
+86-1082649073
cfang@iphy.ac.cn
Citizenship
China
Education
Oct. 2011 Ph.D. Purdue University (USA)

Citation for the Award (within 30 words)

For developing the theory of topological classification and diagnosis for non-magnetic materials.

Description of the work

The research on topological materials is one of the major topics in condensed matter physics. These materials are known to host interesting phenomena such as the negative linear magnetoresistance in the bulk of topological semimetals, and the robust, gapless modes on the surface of topological insulators. The nominee and his group have solved two important problems in this field, the problems of "classification" and "diagnosis".

A key concept in this field is the "topological invariant", a global quantum number that distinguishes topological materials from non-topological ones, and distinguishes different types of topological materials. In fact, all topology-related phenomena in a material are fully determined by this quantum number(s). The types and forms of all topological invariants depend and only depend on two factors: symmetry and dimensionality. Identifying all invariants for a given dimension and symmetry group of interest is, therefore, an important mission for theorists, known as the "classification problem".

The nominee's recent work in Ref.[1,2] for the first time identifies four new Z_2 topological invariants in 3D for the following spatial symmetries: rotation, screw rotation, roto-reflection and inversion. These new invariants in hand and, using a theoretical tool called "layer construction", in Ref.[2] they list all independent topological invariants when the symmetry is time reversal plus any one of the 230 space groups in 3D, solving the classification problem for the cases that are most relevant in condensed matter physics. In Ref.[1], the nominee also for the first time proposes

the presence of "high-order" topological states in 3D, now a new and thriving direction in this field.

While classification is a purely theoretical topic, the "diagnosis problem" is more concerned with realistic materials: it asks for a given real material what are the actual values of the above invariants, based on first-principle calculations. Direct computation of topological invariants is notoriously difficult in many real materials, and this difficulty has so far been hindering the discovery of more topological materials. In Ref.[2], nominee and his group develop a new method that greatly simplifies the calculation, by which people can extract most information on topology only from the symmetry eigenvalues of the bands at several high-symmetry momenta in the Brillouin zone. Based on this method, they in Ref.[3] design an automated diagnosis process that automatically and efficiently finds all topological properties for any given non-magnetic material. This process is then applied to ~40000 materials in a materials database in Ref.[3], and they predict ~8000 materials to be topological semimetals and insulators, exceeding by an order of magnitude the total number of such materials theoretically discovered in the past ten years. The work does not fully solve the diagnosis problem and the method has its limits, but it still marks so far the biggest step forward in this direction.

Key references (up to 3 key publications*)

1. Z. Song, Z. Fang and C. Fang, "*(d-2)-Dimensional Edge States of Rotation Symmetry Protected Topological States*", Phys. Rev. Lett. **119**, 246402 (2017).
2. Z. Song, T. Zhang, Z. Fang and C. Fang, "*Quantitative mappings between symmetry and topology in solids*", Nature Communications **9**, 3530 (2018).
3. T. Zhang, Y. Jiang, Z. Song, H. Huang, Y. He, Z. Fang, H. Weng and C. Fang, "*Catalogue of Topological Electronic Materials*", Nature **566**, 475 (2019).

*) Copy of one most significant publication should be attached.

Nominator (name, affiliation, email, telephone and relation to the candidate)

Name: Hongming WENG

Affiliation: Institute of Physics, Chinese Academy of Sciences

Address: Institute of Physics, Chinese Academy of Sciences P.O.Box 603, Beijing 100190, China

Phone: +86-10-6284-9941 (office); +86-138-1157-0964(cell)

Fax: +86-10-6255-3698

Email: hmweng@iphy.ac.cn

Relation to the candidate: colleague

Signature Date

$(d-2)$-Dimensional Edge States of Rotation Symmetry Protected Topological States

Zhida Song,[1,2] Zhong Fang,[1,3] and Chen Fang[1,*]
[1]*Beijing National Laboratory for Condensed Matter Physics and Institute of Physics, Chinese Academy of Sciences, Beijing 100190, China*
[2]*University of Chinese Academy of Sciences, Beijing 100049, China*
[3]*Collaborative Innovation Center of Quantum Matter, Beijing 100084, China*

(Received 14 August 2017; revised manuscript received 1 October 2017; published 11 December 2017)

We study fourfold rotation-invariant gapped topological systems with time-reversal symmetry in two and three dimensions ($d = 2, 3$). We show that in both cases nontrivial topology is manifested by the presence of the $(d-2)$-dimensional edge states, existing at a point in 2D or along a line in 3D. For fermion systems without interaction, the bulk topological invariants are given in terms of the Wannier centers of filled bands and can be readily calculated using a Fu-Kane-like formula when inversion symmetry is also present. The theory is extended to strongly interacting systems through the explicit construction of microscopic models having robust $(d-2)$-dimensional edge states.

DOI: 10.1103/PhysRevLett.119.246402

Introduction.—A symmetry protected topological state (SPT) is a gapped quantum state that cannot be continuously deformed into a product state of local orbitals without symmetry breaking [1–3]. The SPT is known to have gapless boundary states in one lower dimension [4], i.e., the $(d-1)$-dimensional edge, such as the spin-1/2 excitations at the end of a Haldane chain [5] or the Dirac surface states at the surface of a topological insulator [6,7]. The gapless states are protected by the symmetries on the $(d-1)$-dimensional edge, and when the symmetry is a spatial symmetry, they appear only on the boundary that is invariant under the symmetry operation [8–11].

Very recently, the possibility of having a gapped $(d-1)$-dimensional edge but a gapless $(d-2)$-dimensional edge has been discussed [12–15]. In Ref. [12], it was shown that, in a 2D spinless single-particle (i.e., no spin-orbit coupling) system that has anticommuting mirror planes, all four side edges can be gapped without symmetry breaking on an open square, but there are four modes localized at the four corners (0D edge) protected by mirror symmetries. Here we first extend the theory of 0D-edge states to spin-1/2 fermion systems without mirror symmetries but with fourfold rotation symmetry and time-reversal symmetry. We point out that the presence of 0D-edge states can be understood as the result of a mismatch between the locations of the centers of the Wannier states and those of atoms. Then we generalize the theory to 3D and define a new topological invariant by classifying the "spectral flow" of the Wannier centers between the $k_z = 0$ and the $k_z = \pi$ slices in the Brillouin zone. When this invariant is nontrivial, there are four helical edge modes on the otherwise gapped side surfaces of the 3D system. We further show that, when space inversion is also present, there is a Fu-Kane-like formula [16] relating this invariant to certain combinations of rotation and inversion eigenvalues of the filled bands at high-symmetry crystal momenta. Finally, we generalize the theory to strongly interacting systems, by constructing microscopic models of boson and fermion SPT states that have $(d-2)$-dimensional edge states for $d = 2, 3$ using coupled wire construction. We remark that these edge states, protected by C_4 and some local symmetry such as time reversal, are not pinned to the corners or hinges of the system and can even appear in geometries having smooth side surfaces.

Mismatch between the atom sites and the Wannier centers.—Wannier functions for the filled bands can be constructed for all 2D gapped insulators that have a zero Chern number [17]. When symmetries are involved (time reversal and/or spatial), the set of Wannier functions may or may not form a representation of the symmetry group [18]. If they do, then we call these Wannier functions "symmetric." If a set of symmetric Wannier functions cannot be found for all filled bands, we know that the system cannot be adiabatically deformed into an atomic insulator: This is considered a generalized definition of topologically nontrivial insulators [19,20], since atomic orbitals automatically form a set of symmetric wave functions. Atomic insulators are usually considered trivial. Nevertheless, we realize that even they can also be somewhat nontrivial if there is a mismatch between the Wannier centers and the atomic positions, as shown in the left panel in Fig. 1(a). A Wannier center (WC) can be understood as the middle of the Wannier function (but see Ref. [21] for a rigorous definition), and, if the Wannier functions are symmetric, their centers are also symmetric. When the mismatch happens, it means that, while the insulator can be deformed into some atomic insulator, it would *not* be made by the atoms forming the lattice. The presence of 0D-edge states of the system put on an open disk is the manifestation of the "mismatch."

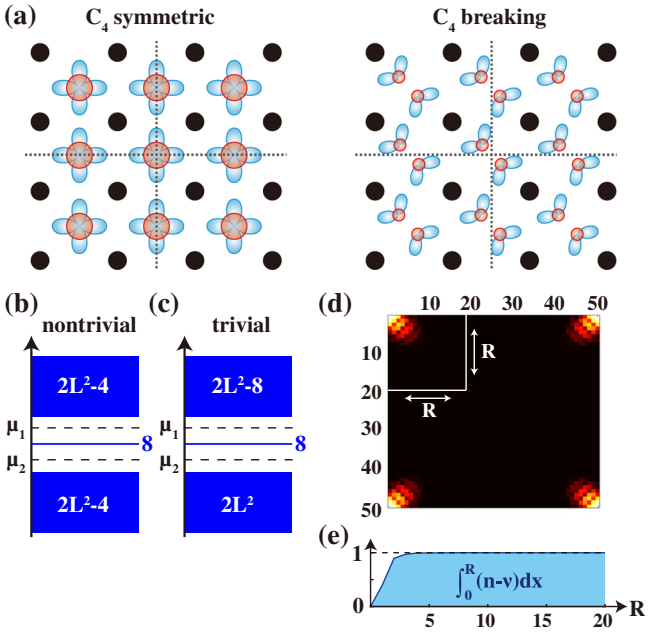

FIG. 1. Nontrivial 0D-edge modes of a 2D fermion. In (a), we sketch the mismatch between the atom sites and the WCs in the presence (left panel) and the absence (right panel) of C_4, where the atom sites are represented by the block circles and the WCs are represented by the colored orbitals. In (b) and (c), level counting for systems with nontrivial and with trivial 0D-edge state is shown, respectively. In (d), the numerical calculated density profile of the 2D model with a finite size of 50×50 is plotted, where the Fermi level is set at μ_1. The four bright regions in (d) show the additional charges located at the corners. To count the number of additional charges around a corner, we plot the integral of the density deviation from the filling ($\nu = 4$) in (e).

To be specific, let us consider a square lattice model

$$H = (1 - \cos k_x - \cos k_y)\tau_0\sigma_z s_0 + \sin k_x \tau_0\sigma_x s_x + \sin k_y \tau_0\sigma_x s_y + \Delta(\cos k_x - \cos k_y)\tau_y\sigma_y s_0, \quad (1)$$

in which all the atomic orbitals are put on the lattice sites. Here τ_i and σ_i ($i = 0, x, y, z$) are Pauli matrices representing the orbital degrees of freedom, and s_i ($i = 0, x, y, z$) representing the spin. This model can be thought of as two copies of 2D topological insulator plus a mixing term with Δ as the coefficient; and it has time-reversal symmetry $T = -is_y K$ and a rotation symmetry $C_4 = \tau_z e^{-i\pi s_z/4}$. The system put on a torus is fully gapped, because the four terms in Eq. (1) anticommute with each other and their coefficients do not vanish at the same time.

As shown in Ref. [21], whatever value Δ takes, the insulator is equivalent to an atomic one, and its WCs are located at the plaquette centers. We have explicitly constructed a set of symmetric Wannier functions and prove that, protected by the time-reversal and C_4 symmetries, the Wannier centers stay invariant under any gauge transformation that keeps the Wannier functions symmetric. This model hence realizes the mismatch between the WCs at plaquette centers and the atomic positions at sites.

Now we cut along the dotted lines in the left panel in Fig. 1(a) and turn the 2D torus into an open square. Since this cut preserves C_4 symmetries, the states centered at the plaquette center will be equally divided into four quarters, so that each quarter carries one extra electron on top of some even integer filling. Because of T, this means that a pair (Kramers's pair) of zero modes are located near each of the four corners of the square. One may observe that, in the absence of particle-hole symmetry (which is an accidental symmetry of the model), the modes can be moved away from zero and pushed into the bulk states, but we argue that, even when this happens, the corners are still nontrivial in the following sense. The total eight modes (two near each corner) come from both the conduction and the valence bands, each having $(N_{\text{band}} - \nu)L^2 - 4$ and $\nu L^2 - 4$ electrons, respectively, where $N_{\text{band}} \in$ even and $\nu \in$ even are the total number of bands and the filling number, respectively, and L the length of the square [Fig. 1(b)]. No matter where the Fermi energy is, a gapped ground state must have 4 mod 8 electrons on an even-by-even lattice, so that each corner has exactly one (or minus one) extra electron on top of the filling of the bulk. This is in sharp contrast with the systems having trivial corner states, whose energy levels are plotted in Fig. 1(c). In that case, the in-gap states can be pushed into the conduction bulk, and there is no extra charge at each corner. In Figs. 1(d) and 1(e), we plot the charge density at $\mu = \mu_1$ in real space and plot the extra electric charge within a small area near the corner as a function of radius in the Slater-product many-body ground state.

To see how the odd parity of the corner charge is protected by C_4, we contrast the above scenario with the one having a nematic perturbation breaking C_4 down to C_2, so that the Wannier centers are shifted to the positions shown in the right panel in Fig. 1(a). When the system is cut along the dotted lines, the quarter has inside it an integer number of Kramers' pairs, and the degeneracy at each corner is absent.

1D helical state and $\mathbb{Z}_2$ Wannier center flow.—A natural generalization of the 0D state in 2D is the 1D-edge state in 3D, where both the 3D bulk and 2D side surfaces are insulating, as shown in Fig. 2(c). Our construction of this state is also based on the WC picture. Assuming the 3D system has T and C_4 symmetries, we can take a C_4-invariant tetragonal cell and transform the Hamiltonian along the z direction to momentum space. Each slice with fixed k_z can be thought of as a 2D system, wherein the $k_z = 0, \pi$ slices are time reversal and C_4 invariant, while the others are only C_4 invariant. Consider an insulator that has four filled bands, or four WCs for each k_z slice. Because of C_4, the four WCs are related to each other by fourfold rotations; and due to T, at $k_z = 0$ or $k_z = \pi$, two WCs that form a Kramers's pair must coincide. Therefore, at $k_z = 0$

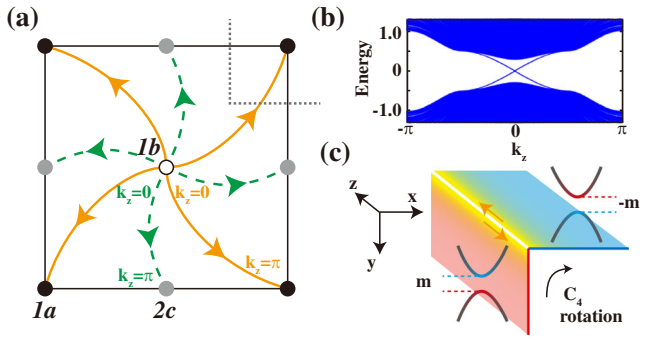

FIG. 2. Nontrivial 1D helical modes of a 3D insulator. In (a), we plot the two generators of nontrivial $\mathbb{Z}_2$ flows from the $k_z = 0$ slice to the $k_z = \pi$ slice, where the lattice site ($1a$), the plaquette center ($1b$), and the edge midpoint ($2c$) are represented by a black planchet, hollow circle, and gray planchet, respectively. In (b), the numerically calculated helical modes of our 3D model on a tetragonal cylinder geometry are plotted. The length along the x and y directions is 50. In (c), we sketch the domain wall between surfaces of opposite masses, enforced by the C_4 rotation symmetry.

and $k_z = \pi$, there are only three possible configurations for the four WC: all four at $1a$, all four at $1b$, and two at each $2c$ Wyckoff position. Wyckoff positions are points in a lattice that are invariant under a subgroup of the lattice space group. For a square lattice in a Wigner-Seitz unit cell, $1a$ and $1b$ are the center and the corner invariant under C_4, $2c$ are the middles of the edges invariant under C_2, and $4d$ are generic points invariant under identity (the trivial subgroup). If the configurations at $k_z = 0$ and at $k_z = \pi$ are different, the evolution of the WC between the two slices forms a "$\mathbb{Z}_2$ flow," a robust topological structure revealing that the 3D insulator is not an atomic one. Out of several different combinations of the configurations at $k_z = 0$ and $k_z = \pi$, there are two topologically distinct $\mathbb{Z}_2$ flows, where the four WCs flow from $1b$ to $1a$ and from $1b$ to $2c$ [solid yellow and dashed green lines in Fig. 2(a)], respectively. The latter $\mathbb{Z}_2$ flow can be shown equivalent to a weak topological index (Ref. [21]), and we from now on focus on the first $\mathbb{Z}_2$ flow from $1b$ to $1a$. Whether this flow is present or not gives us a new $\mathbb{Z}_2$ invariant, and its edge manifestation is the existence of 1D helical edge modes on the side surface of a bulk sample. (For a more rigorous definition and classification of the WC flow for an arbitrary number of filled bands, see Ref. [21].)

To see this bulk-edge correspondence, we cut the bulk along both the x and y directions, keeping the periodic boundary condition along z. From a top-down perspective, a corner of the sample takes the shape of the dotted lines shown in Fig. 2(a). One can see that, at the corner, the boundary cuts through exactly one (or three) line(s) in the WC flow, corresponding to one helical mode along the hinge between the two open surfaces. To make the picture more concrete, we consider the following 3D model, which is a simple extension of the 2D model in Eq. (1):

$$H = \left(2 - \sum_i \cos k_i\right)\tau_0\sigma_z s_0 + \sum_i \sin k_i \tau_0 \sigma_x s_i + \Delta(\cos k_x - \cos k_y)\tau_y\sigma_y s_0. \quad (2)$$

The $k_z = 0$ slice is equivalent with the 2D model in Eq. (1), thus having four charges locating at the plaquette center. The $k_z = \pi$ slice is, however, a 2D atomic insulator with four charges locating at the lattice site. The mismatch between the WCs at $k_z = 0$ and $k_z = \pi$ slices means that the $\mathbb{Z}_2$ flow exists. To confirm the $\mathbb{Z}_2$ flow, we also choose a smooth gauge for all the k_z slices from $k_z = 0$ to $k_z = \pi$ and plot the WC flow explicitly, which indeed gives the $\mathbb{Z}_2$ flow, shown in Ref. [21]. The 1D helical state is also confirmed by a numerical calculation of the band structure of a finite tetragonal cylinder, as plotted in Fig. 2(b). For this particular model, the helical edge states can be viewed from another perspective. The edge between the two open surfaces can be considered as the domain wall between them. On each surface there is a mass gap, and the rotation symmetry in this model enforces the two masses to be opposite, so that at the domain wall there is a helical mode [11] [see Fig. 2(c) for a schematic, and see Ref. [21] for more details].

Symmetry indicators for the $\mathbb{Z}_2$ invariant.—To see if a given insulator has 1D helical edge modes on the side surface, one needs to calculate the evolution of the WCs as a function of k_z, which in turn requires finding symmetric, smooth, and periodic Bloch wave functions for all bands at each k_z slice as is done for our model Hamiltonian. This is practically impossible in real materials. Now we show that, in the presence of additional inversion symmetry, this $\mathbb{Z}_2$ invariant can be determined by the rotation and inversion eigenvalues at all high-symmetry momenta, simplifying the diagnosis. We call this method a "Fu-Kane-like formula," likening it to the Fu-Kane formula for time-reversal topological insulators [16], where inversion is not required to protect the nontrivial topology but when present greatly simplifies the calculation.

This formula is derived based on the new theory of symmetry indicators [19,20]: Given any insulator, a full set of eigenvalues of the space group symmetry operators for filled bands at all high-symmetry points generates a series of indicators. They tell us if this set is consistent with any atomic insulator, and, if yes, the theory further gives where the atomic orbitals are located. Our goal is to find such an indicator that is equivalent to the $\mathbb{Z}_2$ invariant for the WC flow. Following the WC flow picture, we require (i) at $k_z = 0$ and $k_z = \pi$, the eigenvalues of C_4, $C_2 = C_4^2$ and P are consistent with atomic insulators; (ii) there is no surface state on the side surfaces; and (iii) comparing the two slices at $k_z = 0$ and $k_z = \pi$, the numbers of atomic orbitals at $1a$ and at $1b$ change by ± 4 and ∓ 4, respectively. For a concrete example, let us consider space group $P4/m$, whose indicators form a group $\mathbb{Z}_2 \times \mathbb{Z}_4 \times \mathbb{Z}_8$ [19], so that

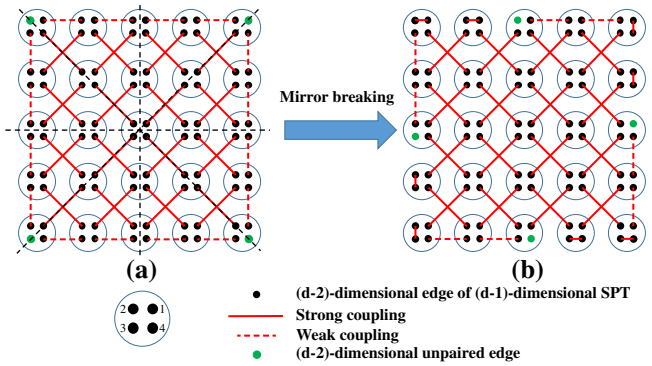

FIG. 3. Coupled wire construction for a 3D SPT with robust 1D-edge modes. Each filled circle is a wire from the top down, and each open circle including four elementary wires is a "physical" wire that can be realized in 1D lattice models. The breaking of mirror symmetry in (a) causes the edge modes to move to the positions in (b).

the insulator according to its C_4 and P eigenvalues can be denoted by (mnl) $(m = 0, 1, n = 0, 1, 2, 3, l = 0, 1, \ldots, 7)$, and an insulator with a nonzero indicator cannot be adiabatically deformed into an atomic insulator. Using the three criteria above, we find that the $\mathbb{Z}_2$ flow is nontrivial only if $(mnl) = (004)$. We have found the explicit formulas to calculate these indicators directly from the symmetry eigenvalues, which can be applied to all space groups having both C_4 and P. (See Ref. [21] for the results, and find a MATLAB script therein for an automated diagnosis for materials in these space groups.)

Extension to strongly interacting SPT.—In the above we have established the theory of $(d-2)$-dimensional edge modes for free fermions through the WC picture. Since WC is a single-particle object, the same picture does not apply for strongly interacting bosons or fermions. Here we rebuild a 3D free fermion model with robust 1D helical edge modes using coupled wire construction [24–28], a method that can be easily extended to strongly interacting SPT. These SPT can either be bosonic [29] or fermionic and are, in general, protected by spatial symmetry [30] plus some internal symmetry [31].

Consider an arrangement of 1D wires shown in the top down view in Fig. 3(a), each of which represents a helical mode. Because of the fermion doubling theorem, each wire alone cannot be physically realized in 1D, but an even number of these wires can be realized as a 1D wire fine-tuned to a critical point. In our model, four wires make a physical, critical 1D wire. For concreteness, we assume that under C_4 rotation the four wires inside cyclically permute. Then we couple the wires in the following way: The four wires, in the top down view, which share a plaquette are coupled diagonally, i.e., 1 coupled to 3 and 2 to 4. For a 3D torus, these couplings (solid red lines) make the coupled wire system an insulator. For a cylinder geometry open in the x and y directions, however, there are "dangling helical wires" on the side surfaces, which can again be gapped by turning on a dimerizing coupling (dotted lines). But one soon discovers that, as long as C_4 is preserved, there are always four unpaired wires on the side surface (represented by green dots), which are in fact the same 1D helical edge mode protected by C_4 and T studied above.

This construction can be easily extended to strongly interacting SPT. One simply replaces each helical wire with a $(d-2)$-dimensional edge of a $(d-1)$-dimensional SPT protected by some local symmetry. For example, each "wire" can be a 0D spin $1/2$, which is the edge of a 1D Haldane chain protected by SO(3) symmetry. In that case, the resultant construction in Fig. 3(a) is nothing but an Affleck-Kennedy-Lieb-Tasaki (AKLT)-like state [32,33] formed by $S = 2$ spins, but, unlike previously considered AKLT states in 2D, it has a gapped 1D edge but four 0D gapless spin-$1/2$ excitations localized at the four corners in an open square. We can also replace each wire by the edge of a Levin-Gu state [34], protected by a $\mathbb{Z}_2$ local symmetry, and then the construction in Fig. 3(a) is a 3D bosonic SPT with 1D gapless modes at four corners. Notice that, in these boson examples, time-reversal symmetry is not necessary. Similar construction can be used to obtain SPT states protected by both the local symmetries [being T, SO(3), or Z_2] and C_4-rotation symmetry.

Discussion.—It is important to note that, while in examples studied so far the $(d-2)$-dimensional edge modes sit at the corners or hinges in the disk or cylinder geometry, it is not always the case. In the model shown in Fig. 3(a), the edge modes are pinned to the corners by the mirror symmetries (dotted lines), and breaking these mirror planes in the bulk or on the surface causes the edge modes to move away. In the example shown in Fig. 3(b), we break the mirror symmetry of the construction on the surface, so that the dangling wires move from the corners to some generic points on the side. As long as C_4 is present, the $(d-2)$-dimensional edge modes are stable yet not pinned to corners or hinges in the absence of mirror symmetries. In fact, they still appear even if the whole side surface is smooth without hinges at all. We also emphasize that, while these edge modes are protected by C_4-rotation symmetry, breaking the symmetry perturbatively in the bulk or on the boundary does not, in general, gap out the modes, because time reversal alone is sufficient to protect 1D helical edge modes. The only way of gapping the modes is to annihilate them in pairs, and this means large C_4 breaking either in the bulk or on the boundary. Similar discussions may be extended to systems with twofold, threefold, and sixfold rotations.

Experimentally, the four helical edge modes of a 3D electronic insulator contribute a quantized conductance of $4e^2/h$ that may be measured in electric transport [7]. Also, the $(d-2)$-dimensional edge modes may be detected by local probes such as scanning tunneling microscopy, either on a bulk sample or at the step edge of a thin film.

C. F. thanks Xi Dai, Meng Cheng, Yang Qi, and B. Andrei Bernevig for helpful discussion. The work was

supported by the National Key Research and Development Program of China under Grant No. 2016YFA0302400 and by National Science Foundation of China under Grant No. 11674370.

Note added.—We are aware of works on related topics that have appeared on arXiv after our posting [35–37]; their results have a finite overlap with ours and seem consistent.

*cfang@iphy.ac.cn

[1] Z.-C. Gu and X.-G. Wen, Phys. Rev. B **80**, 155131 (2009).
[2] X. Chen, Z.-C. Gu, Z.-X. Liu, and X.-G. Wen, Science **338**, 1604 (2012).
[3] Y.-M. Lu and A. Vishwanath, Phys. Rev. B **86**, 125119 (2012).
[4] X. Chen, Z.-X. Liu, and X.-G. Wen, Phys. Rev. B **84**, 235141 (2011).
[5] F. D. M. Haldane, Phys. Rev. Lett. **50**, 1153 (1983).
[6] M. Z. Hasan and C. L. Kane, Rev. Mod. Phys. **82**, 3045 (2010).
[7] X.-L. Qi and S.-C. Zhang, Rev. Mod. Phys. **83**, 1057 (2011).
[8] L. Fu, Phys. Rev. Lett. **106**, 106802 (2011).
[9] A. M. Turner, Y. Zhang, and A. Vishwanath, Phys. Rev. B **82**, 241102 (2010).
[10] T. L. Hughes, E. Prodan, and B. A. Bernevig, Phys. Rev. B **83**, 245132 (2011).
[11] T. H. Hsieh, H. Lin, J. Liu, W. Duan, A. Bansil, and L. Fu, Nat. Commun. **3**, 982 (2012).
[12] W. A. Benalcazar, B. A. Bernevig, and T. L. Hughes, Science **357**, 61 (2017).
[13] F. Schindler, A. Cook, M. G. Vergniory, and T. Neupert, in Proceedings of the APS March Meeting (unpublished).
[14] R.-J. Slager, L. Rademaker, J. Zaanen, and L. Balents, Phys. Rev. B **92**, 085126 (2015).
[15] Y. Peng, Y. Bao, and F. von Oppen, Phys. Rev. B **95**, 235143 (2017).
[16] L. Fu, C. L. Kane, and E. J. Mele, Phys. Rev. Lett. **98**, 106803 (2007).
[17] N. Marzari and D. Vanderbilt, Phys. Rev. B **56**, 12847 (1997).
[18] A. A. Soluyanov and D. Vanderbilt, Phys. Rev. B **83**, 035108 (2011).
[19] H. C. Po, A. Vishwanath, and H. Watanabe, Nat. Commun. **8**, 50 (2017).
[20] B. Bradlyn, L. Elcoro, J. Cano, M. G. Vergniory, Z. Wang, C. Felser, M. I. Aroyo, and B. A. Bernevig, Nature (London) **547**, 298 (2017).
[21] See Supplemental Material at http://link.aps.org/supplemental/10.1103/PhysRevLett.119.246402 for derivation of the topological invariants, the detailed analysis of our toy model, and derivation of the Fu-Kane-like formula, which includes Refs. [22,23].
[22] S. L. Altmann and P. Herzig, *Point-Group Theory Tables* (Clarendon, Oxford, 1994).
[23] C. Fang, M. J. Gilbert, and B. A. Bernevig, Phys. Rev. B **86**, 115112 (2012).
[24] J. C. Y. Teo and C. L. Kane, Phys. Rev. B **89**, 085101 (2014).
[25] Y. Oreg, E. Sela, and A. Stern, Phys. Rev. B **89**, 115402 (2014).
[26] T. Neupert, C. Chamon, C. Mudry, and R. Thomale, Phys. Rev. B **90**, 205101 (2014).
[27] J. Klinovaja and Y. Tserkovnyak, Phys. Rev. B **90**, 115426 (2014).
[28] J. Klinovaja, Y. Tserkovnyak, and D. Loss, Phys. Rev. B **91**, 085426 (2015).
[29] R. Thorngren and D. V. Else, arXiv:1612.00846.
[30] S.-J. Huang, H. Song, Y.-P. Huang, and M. Hermele, arXiv:1705.09243 [Phys. Rev. B (to be published)].
[31] C. Wang and M. Cheng (to be published).
[32] I. Affleck, T. Kennedy, E. H. Lieb, and H. Tasaki, Phys. Rev. Lett. **59**, 799 (1987).
[33] I. Affleck, T. Kennedy, E. H. Lieb, and H. Tasaki, Commun. Math. Phys. **115**, 477 (1988).
[34] M. Levin and Z.-C. Gu, Phys. Rev. B **86**, 115109 (2012).
[35] W. A. Benalcazar, B. A. Bernevig, and T. L. Hughes, Phys. Rev. B **96**, 245115 (2017).
[36] F. Schindler, A. M. Cook, M. G. Vergniory, Z. Wang, S. S. P. Parkin, B. A. Bernevig, and T. Neupert, arXiv:1708.03636.
[37] J. Langbehn, Y. Peng, L. Trifunovic, F. von Oppen, and P. W. Brouwer, preceding Letter, Phys. Rev. Lett. **119**, 246401 (2017).

nature COMMUNICATIONS

ARTICLE

DOI: 10.1038/s41467-018-06010-w OPEN

Quantitative mappings between symmetry and topology in solids

Zhida Song[1,2], Tiantian Zhang[1,2], Zhong Fang[1] & Chen Fang[1,3]

The study of spatial symmetries was accomplished during the last century and had greatly improved our understanding of the properties of solids. Nowadays, the symmetry data of any crystal can be readily extracted from standard first-principles calculation. On the other hand, the topological data (topological invariants), the defining quantities of nontrivial topological states, are in general considerably difficult to obtain, and this difficulty has critically slowed down the search for topological materials. Here we provide explicit and exhaustive mappings from symmetry data to topological data for arbitrary gapped band structure in the presence of time-reversal symmetry and any one of the 230 space groups. The mappings are completed using the theoretical tools of layer construction and symmetry-based indicators. With these results, finding topological invariants in any given gapped band structure reduces to a simple search in the mapping tables provided.

[1] Beijing National Research Center for Condensed Matter Physics, and Institute of Physics, Chinese Academy of Sciences, Beijing 100190, China. [2] University of Chinese Academy of Sciences, Beijing 100049, China. [3] CAS Center for Excellence in Topological Quantum Computation, Beijing 100190, China. Correspondence and requests for materials should be addressed to C.F. (email: cfang@iphy.ac.cn)

Distinct phases do not always differ from each other in their symmetries as expected in the Ginzburg-Landau paradigm. Two gapped phases having the same symmetry may be distinguished by a set of global quantum numbers called topological invariants[1–8]. These invariants are quantized numbers, whose types (integer, Boolean, and others) only depend on the symmetry group and the dimension of the system[9,10]. The invariants fully characterize topological properties that are unchanged under arbitrary adiabatic tuning of the Hamiltonian that preserves the relevant symmetry group. Materials having non-zero topological invariants are loosely called topological materials (whereas the technical term is symmetry protected topological states[11–13]), a new kind of quantum matter that hosts intriguing physical observables such as quantum anomaly on their boundaries[14–16], and are considered candidate materials for new quantum devices[17–21]. Success in finding these materials largely depends on the numerical evaluation (prediction) of the topological invariants in a given candidate material. However, even for electronic materials having weak electron correlation, where the topological invariants are best understood and expressed in terms of the wave functions of the valence bands, these calculations still prove quite challenging. In fact, numerically finding a new topological material has proved so hard that a single success[17,22–25] would have triggered enormous interest[26–32].

On the other hand, mathematicians and physicists have since long developed, via the representation theory of space groups, a complete toolkit for the study of the symmetry properties of bands in solids[33,34]. Given any point in momentum space, each energy level corresponds to an irreducible representation (irreps) of the little group at that momentum, depending on the Blöch wave functions at the level. Modern implementations of the density functional theory output both the energy levels and their Blöch wave functions for any given crystal momenta, such that finding the irreps of all valence bands in a band structure (BS) is now considered a solved problem that can be automated.

It has been eagerly hoped that quantitative relations exist between the topological invariants and the irreps in the valence bands at high-symmetry points in the Brillouin zone, i.e., the symmetry data of valence bands. These relations, if existed, would reduce the difficult task of finding the former to a routine calculation of the latter. However, the examples are rare[35–38]. Fu-Kane formula[35] for topological insulators protected by time-reversal symmetry (TI for short from now) is an exemplary one, mapping the four topological $\mathbb{Z}_2$-invariants to inversion eigenvalues at eight high-symmetry points. This simple golden rule considerably expedited the search for TI in all centrosymmetric materials via first-principles numerics[22]. Nevertheless, for general topological states in three dimensions protected by any one of the 230 space groups with and without time-reversal, or topological crystalline insulators[39] (TCIs), explicit formulae relating their topological invariants to symmetry data have so far been missing.

Recently, a solid step along this direction is made in refs. [40–43], where the authors systematically study the connectivity of bands in a general gapped BS and identify the constraints on the symmetry data in the form of linear equations called the compatibility equations. ref. [41] explicitly provides these relations for each space group and observes that if a symmetry data satisfying all compatibility relations cannot decompose into elementary band representations (sets of symmetry data of atomic insulators (AIs), given in the same paper), the material must be topologically nontrivial. ref. [40] shows that the symmetry data of any gapped BS can be compressed into a set of up to four $\mathbb{Z}_{n=2,3,4,6,8,12}$ numbers called symmetry-based indicators (SIs) (see Methods section for a brief review of SI). The set of SI is a lossless compression of symmetry data as far as topological invariants are concerned: all topological invariants that may be extracted from symmetry data can be inferred from the corresponding SI. The theory presented in ref. [40] does not, however, relate SI to the topological invariants, the defining quantities of topological states: a BS having non-zero SI is necessarily topological, but the type of the topology in terms of invariants is unknown. The explicit expressions of the SI in terms of symmetry data are also missing in ref. [40].

This paper aims to complete the mapping between symmetry data and topological invariants in systems with time-reversal symmetry and significant spin–orbital coupling (the symplectic Wigner–Dyson class or class AII in the Altland-Zirnbauer system[44]). To achieve this, we first derive the explicit expression of each SI in all space groups (Supplementary Tables 1–3) and then, given any non-zero set of SI in every space group, we enumerate all possible combinations of topological invariants that are compatible with the SI (Supplementary Tables 4–8). These invariants include: three weak topological invariants $\delta_{w,i=1,2,3}$[8], mirror Chern number C_m[23,45], glide plane (hourglass) invariant δ_h[24], rotation invariant δ_r[21,46,47], the inversion invariant δ_i[21,36,37], a new $\mathbb{Z}_2$ topological invariant protected by screw rotations δ_s, and finally a new $\mathbb{Z}_2$ topological invariant protected by S_4-symmetry δ_{S_4}. The last two invariants are theoretically established in Supplementary Note 1. In the main results, the strong time-reversal invariant δ_t[8] is assumed to vanish, so that the results are restricted to TCI only, or states that can be adiabatically brought to AIs in the absence of crystalline symmetries; the $\delta_t = 1$ cases are briefly discussed in the end of the Results section. The exhaustive enumeration maps 478 sets of SI to 3133 linearly independent combinations of topological invariants, as tabulated in Supplementary Table 7. A guide for reading this table is offered in Supplementary Note 7.

Results

An example showing the usage of our results. Before entering into the derivation of the results, we use tin telluride (SnTe) crystal having space group $Fm\bar{3}m$ (#225) to illustrate how the results should be used in Fig. 1. One should first compute the symmetry data of the material, finding the numbers of appearances for each irrep in the valence bands at the high-symmetry momenta, namely, Γ, X, L, and W. This can be done in any modern implementation of first-principles numerics and here we use Vienna ab-initio simulation package[48,49]. From the symmetry data obtained in the top of Fig. 1, we apply the formulae given in Supplementary Tables 1 and 2 to find the SI, which in this case is a single $\mathbb{Z}_8$ number, and we find $z_8 = 4$. After this, we can use Supplementary Table 7 and find that $z_8 = 4$ corresponds to two and only two possible sets of topological invariants shown on the bottom of Fig. 1: it either has non-zero mirror Chern number $C_{m(001)} = 4$ (mod 8) for the $k_z = 0$ plane (and symmetry partners) or has mirror Chern number $C_{m(110)} = 2$ (mod 8) for the $k_x + k_y = 0$ plane (and symmetry partners). It is impossible, however, to distinguish these two cases using symmetry data, but advanced tools such as Wilson loops must be invoked. Further analysis shows that the latter state appears in the real material[23].

Layer construction as an general approach. A remarkable feature of all known TCIs is that any TCI can be adiabatically (without gap closing) and symmetrically tuned into a simple product state of decoupled, identical layers in real space, each of which decorated with some two-dimensional (2D) topological state[21,50–54]. This form of fixed-point wave function for a TCI is called its layer construction (LC). An analogy to AIs can be drawn to help understand the physical nature of LC in the following aspects: although an AI is built from decoupled point-like atoms, the building blocks of an LC are decoupled layers. Each atom in

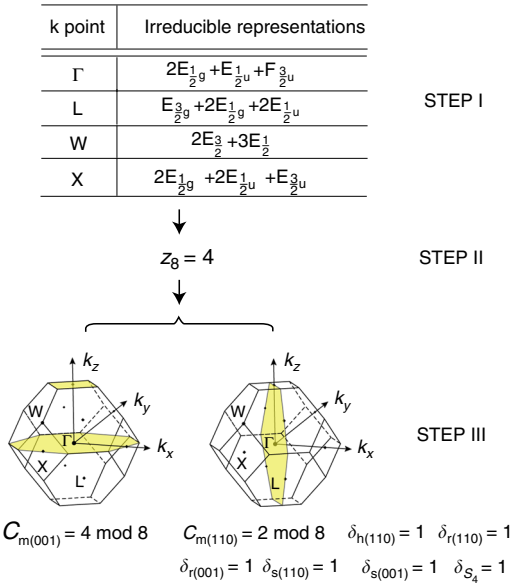

Fig. 1 A demonstration of the diagnosis for tin telluride of space group $Fm\bar{3}m$ (#225) using our results. The table on the top shows the symmetry data obtained in the first-principles calculation (details given in text), where the numbers of appearance of each irrep in the valence bands are listed for each high-symmetry point in the face-centered-cubic Brillouin zone. From the data one finds the SI $z_8 = 4$ using Supplementary Tables 1 and 2, and then by searching for this indicator in Supplementary Table 7, two possible sets of topological invariants are found, listed at the bottom left and bottom right, respectively. The yellow planes in the Brillouin zone are where the mirror Chern numbers $C_{m(001)}$ and $C_{m(110)}$ are defined. Indices in the parentheses in subscript represent the directions of the corresponding symmetry elements. The real material has been shown in ref. [23] to have the topological invariants listed on the bottom right

an AI is decorated with electrons occupying certain atomic orbitals, whereas each layer is decorated with electrons forming a 2D topological state. The atomic orbitals of an atom in lattice correspond to the irreducible representations of the little group at that atomic position, whereas the possible topological states on a layer also depends on the little group leaving the layer invariant. In an LC, there are only two possible decorations: if the layer coincides with some mirror plane of the space group the state for decoration is a 2D mirror TCI with mirror Chern number C_m, and if it does not coincide it is a 2D TI. We define elementary LC (eLC) as an LC generated by a single layer in real space

$$(mnl; d) \equiv \{\mathbf{r}|(m\mathbf{b}_1 + n\mathbf{b}_2 + l\mathbf{b}_3)\cdot\mathbf{r} = 2\pi d \bmod 2\pi\} \qquad (1)$$

Here (mnl) are the Miller indices, and $\mathbf{b}_i$'s the reciprocal lattice vectors; generation here means we take all elements $g \in G$ to obtain the set of layers $E(mnl; d) \equiv \{g(mnl; d)|g \in G\}$ by acting g on $(mnl; d)$. Every LC is a superposition of a finite number of eLCs and, thanks to the additive nature of all known topological invariants, the topological invariants of any LC is the sum of the invariants of all constituent eLCs.

For any space group, we exhaustively find all eLCs using the method detailed in Supplementary Note 3. Although the calculation of topological invariants is difficult for an arbitrary BS, it is easy for an eLC, thanks to its simple structure. In fact, the invariants only depend on how many times each symmetry element is occupied (see Supplementary Note 1 for proof, wherein the occupation for glide plane or screw axis is subtle). A symmetry element is a manifold in real space, where each point is invariant under some symmetry operation. It could be a discrete

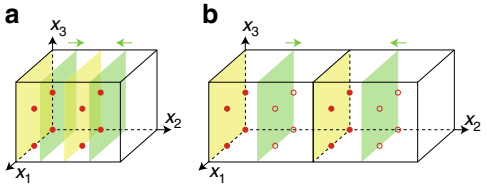

Fig. 2 Layer constructions for space group $P\bar{1}$ (#2). **a** The yellow planes are (010; 0) and (010; $\frac{1}{2}$) respectively, and the two green planes are (010; d) and (010; $1-d$) with $d \neq 0, \frac{1}{2}$. The arrows mean that the two green planes can move towards each other without breaking inversion. **b** After doubling the unit cell along x_2-direction, the open dots are no longer inversion centers as they were, whereas the solid dots remain. Again the arrows mean that two green planes can move towards each other without breaking the inversion symmetry, after unit cell doubling

point such as an inversion center or a center of $S_4 : (x, y, z) \to (-y, x, -z)$, a line such as a rotation axis, or a plane such as a mirror plane. In this way, topological invariants for each eLC are calculated and tabulated in Supplementary Tables 5 and 6. On the other hand, the SI of an eLC are also easily calculated, detailed in Supplementary Note 5 again due to the decoupled nature of the layers. Matching the SI with invariants for each eLC, we hence find the full mapping between SI and topological invariants for TCI. For intuitive understanding, we also plot a set of figures (Supplementary Figs. 1–8) showing the invariants, SI, and phase transitions of eLCs.

From indicators to invariants. Here we take space group $P\bar{1}$ as an example to show the mapping between indicators and invariants and leave the general discussion in the Supplementary Notes 1 and 5. The space group $P\bar{1}$ has non-orthogonal lattice vectors $\mathbf{a}_{i=1,2,3}$ and inversion symmetry. Within a unit cell, there are eight inversion centers at $(x_1, x_2, x_3)/2$ in the basis of lattice vectors (the red solid circles in Fig. 2), where $x_i = 0, 1$. These inversion centers are denoted by $V_{x_1x_2x_3} \equiv (x_1, x_2, x_3)/2 \bmod 1$. A generic layer $(mnl; d)$ is given by $L = \{\mathbf{r}|(m\mathbf{b}_1 + n\mathbf{b}_2 + l\mathbf{b}_3)\cdot\mathbf{r} = 2\pi d \bmod 2\pi\}$, where $d \in [0, 1)$, and at least one of m, n, l is odd (or they would have a common factor). If $d \neq 0, \frac{1}{2}$, we have $d \neq -d \bmod 1$, then under inversion a generated plane $L' = (mnl; 1-d) \neq L$ is a different plane symmetric to L about the origin. In that case, the two planes L and L' can adiabatically move towards each other without breaking any symmetry until they coincide, a process illustrated in Fig. 2a. The state decorated on L and L' are 2D TIs, and due to the $\mathbb{Z}_2$-nature, when L and L' coincide, the resultant double layer becomes topologically trivial. The eLC generated by $(mnl; d \neq 0, \frac{1}{2})$ is hence a trivial insulator. For $d = 0, \frac{1}{2}$, L is invariant under inversion, and always passes four of the eight inversion centers, that is, V_i's that satisfy the equation $mx_1 + nx_2 + lx_3 = 2d \bmod 2$. For examples, if $(mnl; d) = (010; 0)$, then $V_{000,001,100,101}$ are on L (the left yellow plane in Fig. 2a). As each layer is decorated with 2D TI, eLC$(mnl; d)$ $(d = 0, \frac{1}{2})$ is the familiar weak TI having weak invariants

$$\delta_{w,1} = m \bmod 2 \quad \delta_{w,2} = n \bmod 2 \quad \delta_{w,3} = l \bmod 2 \qquad (2)$$

Now we turn to the inversion invariant δ_i, which is a strong invariant robust against all inversion preserving perturbations. Let us consider a perturbation that doubles the periodicity in the (mnl)-direction, whereas preserving the inversion center at origin. After the doubling, four of the eight inversion centers satisfying $mx_1 + nx_2 + lx_3 = 1 \bmod 2$ are no longer inversion centers, so that the plane $(mnl, \frac{1}{2})$ after the doubling no longer passes through any inversion center, and the generated eLC by $(mnl, \frac{1}{2})$ can be

trivialized after the doubling by pairwise annihilating with its inversion partner. Therefore, eLC(mnl, $\frac{1}{2}$) can be trivialized, while keeping the inversion symmetry about the origin, thus having $\delta_i = 0$. In Fig. 2b, we take $(mnl) = (010)$ as an example and doubled the unit cell. We see that the four inversion centers marked by empty circles are not inversion centers in the new cell and the blue plane at (010; $\frac{1}{2}$) in the original cell becomes (010; $\frac{1}{4}$) in the new cell. The two blue planes can move and meet each other at the yellow plane, denoted by (010;$\frac{1}{2}$) in the new cell. The eLC generated by (mnl; 0)-plane, however, passes all eight inversion centers in the enlarged unit cell and cannot be trivialized without breaking inversion (yellow planes in Fig. 2b), so that the inversion invariant $\delta_i = 1$.

After finding the invariants for all possible eLCs, we turn to the SI for each eLC. The SI group of P$\bar{1}$ takes the form $\mathbb{Z}_2 \times \mathbb{Z}_2 \times \mathbb{Z}_2 \times \mathbb{Z}_4$, wherein the first three are the weak TI indicators $z_{2w,i=1,2,3}$ and the last one is the z_4 indicator. The calculation method is briefly described in Supplementary Note 5 and here we only give the results. For eLC(mnl; 0) and eLC(mnl; $\frac{1}{2}$), their values are found to be (m mod 2, n mod 2, l mod 2, 2) and (m mod 2, n mod 2, l mod 2, 0), respectively. For this space group, the mapping from SI set to topological invariants is therefore one-to-one: $z_{2w,i} = \delta_{w,i}$ and $z_4 = 2\delta_i$.

Convention dependence of topological invariants. A subtle but important remark is due at this point. There are always eight inversion centers in a unit cell in the presence of inversion symmetry, and when translation symmetry is broken, only one, two, or four of them remain. In the definition of inversion invariant δ_i, one of the eight is chosen as the inversion center that remains upon translation breaking. In the above example, when the unit cell is doubled, the origin was chosen as the center that remains, but if we chose $V_{010} = (\frac{1}{2}, 0, 0)$, which is a completely valid choice, the four open circles in Fig. 2b are still inversion centers but the solid circles are not after the doubling. In that case, we would find that eLC(mnl, $\frac{1}{2}$) has $\delta_i = 1$ but eLC(mnl, 0) has $\delta_i = 0$. The inversion invariant δ_i hence depends on the convention which one of the eight inversion centers in the unit cell is chosen in the definition of δ_i. However, when we superimpose the two eLCs into an LC that passes all eight inversion centers in a unit cell, the value of δ_i is independent of the choice of the inversion center, as all eight are occupied in this LC. We emphasize that only if this is the case can we hope to observe the physical properties, such as the characteristic boundary states associated with the bulk invariant δ_i[21], because physical observables should not depend on the conventions.

Moreover, similarly, as detailed in Supplementary Note 2, the rotation (screw) invariant $\delta_r = 1$ ($\delta_s = 1$) is convention-independent if and only if each rotation (screw) axis in unit cell is occupied by the LC for $n/2$ mod n times, where $n = 2, 4, 6$ is the order of the rotation (screw) axis. For the S_4 invariant $\delta_{S_4} = 1$ or the hourglass invariant $\delta_h = 1$ to be convention-independent, the LC should occupy each S_4 center or glide plane for an odd number of times. Invariants that are convention-independent are marked blue in Supplementary Tables 7 and 8.

The one-to-many nature of the mapping. In the example of space group P$\bar{1}$, the mappings between indicators and topological invariants are one-to-one. However, this is in fact the only space group where mappings are bijective. By definition, different sets of indicators must correspond to different sets of invariants, but multiple sets of invariants may correspond to the same set of indicators, i.e., the mapping from indicators to invariants is one-to-many.

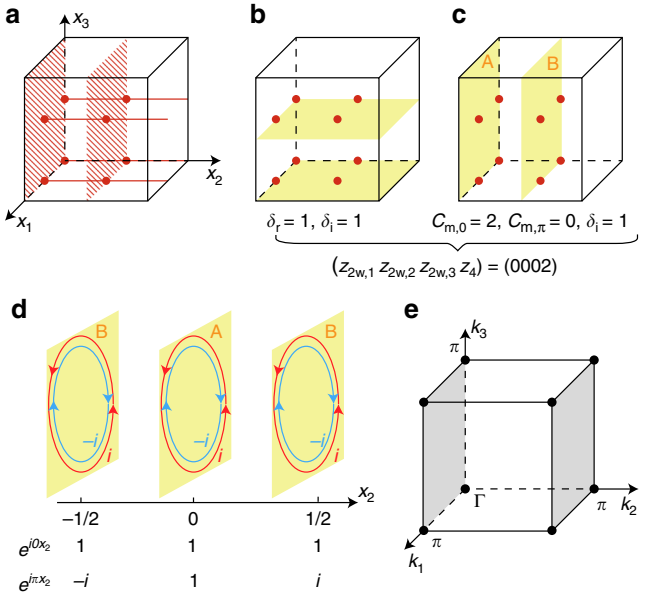

Fig. 3 Two layer constructions for space group $P2/m$, sharing the same set of SI of (0002). **a** All symmetry elements of the space group in one unit cell, including eight inversion centers (red solid circles), four rotation axes (red solid lines), and two mirror planes (shaded planes). **b**, **c** LC1 and LC2 defined in the text, respectively. They have distinct topological invariants but identical indicators. **d** 3D Blöch wave functions in LC2 as superpositions of 2D Blöch wave functions with coefficients $e^{ik_2x_2}$. Here we use red and blue loops to represent the 2D wave functions having mirror eigenvalues i and $-i$, respectively, wherein i wave functions have Chern number 1 and $-i$ wave functions have Chern number −1. For A-eLC the 3D Blöch wave functions at $k_2 = 0$ and $k_2 = \pi$ have the same mirror eigenvalues, leading to identical mirror Chern numbers at $k_2 = 0$ and $k_2 = \pi$. Although for B-eLC the Blöch wave functions at $k_2 = 0$ and $k_2 = \pi$ have opposite mirror eigenvalues, leading to opposite mirror Chern numbers at $k_2 = 0$ and $k_2 = \pi$. **e** The two mirror-invariant planes (gray planes) in Brillouin zone

To understand the one-to-many nature of the mapping more concretely, we look at the specific group $P2/m$, containing two mirror planes, four C_2-axes and eight inversion centers in each unit cell, all marked in Fig. 3a. Now we consider two different LCs illustrated in Fig. 3b, c: in Fig. 3b for LC1, two horizontal planes, each decorated with a 2D TI, occupy all four C_2-axes and all eight inversion centers, and in Fig. 3c for LC2, two vertical planes, each decorated with a mirror Chern insulator with $C_m = 1$, occupy the two mirror planes and the eight inversion centers.

As all inversion centers are occupied in LC1 and LC2, in both cases we have $\delta_i = 1$. LC1 occupies all four C_2-rotation axes, once each, thus having nontrivial rotation invariant $\delta_r = 1$, whereas LC2 does not occupy any of the rotation axes, having $\delta_r = 0$. On the other hand, LC2 occupies the two mirror planes, each with 2D TCI having $C_m = 1$. According to the calculation in Method section LC2 has mirror Chern numbers $C_m = 2$ at $k_z = 0$ plane and $C_m = 0$ at $k_z = \pi$ plane; LC1, not occupying any mirror plane, has vanishing mirror Chern number. LC1 and LC2 are therefore topologically distinct states.

Now we turn to the SI of LC1 and LC2. For space group $P2/m$, the SI have the same group structure $\mathbb{Z}_2 \times \mathbb{Z}_2 \times \mathbb{Z}_2 \times \mathbb{Z}_4$ as that of its subgroup P$\bar{1}$. In this case, the value of each indicator remains the same as we break the symmetry down to P$\bar{1}$. Viewed as LC in P$\bar{1}$, both LC1 and LC2 are the superpositions of eLC(mnl, 0) and eLC(mnl, $\frac{1}{2}$), thus having, by the additivity of SI, $z_{2w,i} = 0$ and $z_4 = 2$.

The failure in distinguishing LC1 and LC2 by indicators reveals a general ambiguity in the diagnosis of mirror Chern numbers. We can add additional even number ($2p$) of A-eLC and even number ($2q$) of B-eLC to LC1 such that the composite state has the same SI and δ_r with LC1 but non-zero mirror Chern numbers $C_{m,0}=2p+2q$, $C_{m,\pi}=2p-2q$. On the other hand, we can also add these additional eLCs to LC2 to get a state having the same SI with LC2 but different mirror Chern numbers $C_{m,0}=2+2p+2q$, $C_{m,\pi}=2p-2q$. The proof here can be generalized to any space group having mirror planes and perpendicular rotation axes, providing that the order of the rotation is even. In all these space groups, as shown in Supplementary Table 7, the TCIs having invariants $\delta_r=1$ and $C_{m,0}-C_{m,\pi}=0$ mod $2n$ and the TCIs having $\delta_r=0$ and $C_{m,0}-C_{m,\pi}=n$ mod $2n$ have the same SI, here n is the order of the rotation axis. The two possible sets of invariants shown in Fig. 1, wherein one is $C_{m(001)}=4$ mod 8, $\delta_{r(001)}=0$ and the other is $C_{m(001)}=0$ mod 8, $\delta_{r(001)}=1$, are the examples for $n=4$.

Indicators for time-reversal topological insulators. In the SI group of each space group, except #174 and #187–190, there is one special indicator of $\mathbb{Z}_{2,4,8,12}$-type, denoted by z_t, marked red in Supplementary Tables 2 and 3. When this special indicator is odd, the system is the well-known three-dimensional (3D) time-reversal topological insulator[40] (TI for short). The essential difference between a TI and a TCI is that the former only requires time-reversal symmetry, such that it remains nontrivial even when all crystalline symmetries are broken. TI does not have LCs, so that the method we use does not apply to SI having $z_t\in$ odd. To construct states having $z_t\in$ odd, we first notice that TI is consistent with all space groups, such that for each space group, we have at least one state that is a TI. Then we can superimpose this TI with all existing LCs obtained, and generate gapped states for all non-zero combinations of SI with $z_t\in$ odd (but with five exceptions discussed in Discussion section).

Regarding $z_t\in$ odd, we comment that the value of z_t generally has a convention dependence on the overall signs in the definition of inversion and the rotation operators. For example, in space group $P\bar{1}$, the defining properties of the symmetry operators are $\hat{P}^2=1$, $\hat{T}^2=-1$ and $[\hat{P},\hat{T}]=0$. It is easy to check that the overall sign in front of $\hat{P}$ can be freely chosen without violating any of the above relations. In other words, without external references, it is unknown a priori if, e.g., an s-orbital should be assigned with positive or negative parity. Upon redefining $\hat{P}\to-\hat{P}$, a state having $z_4=1$ goes to $z_4=3$ and vice versa. In similar ways, it is proved in Supplementary Note 4 that states having the $\mathbb{Z}_8$-indicator $z_8=1, 3, 5, 7$ differ only by convention and so do the states have $\mathbb{Z}_{12}$-indicator $z_{12}=1, 5, 7, 11$. In these cases, the convention refers to the overall sign in front of inversion operator and the sign in front of the rotation operator. It is difficult to distinguish these states from each other experimentally. However, here we emphasize that the SI $z_4=1, 3$ (so do the SI $z_8=1, 3, 5, 7$ and $z_{12}=1, 5, 7, 11$) have a relevant difference under a fixed convention, which can be detected by the anomalous boundary between the two phases. For example, suppose we have a spherical sample of $z_4=3$ phase and fill the space outside the sphere with $z_4=1$ phase, then as long as the geometry keeps inversion symmetry, the boundary state on the spherical surface should be identical with the boundary state between $z_4=2$ and $z_4=0$ phases, which is known as one-dimensional helical mode (see Supplementary Note 1 for details). This is because we can deduct a background of $z_4=1$ phase both inside and outside the sphere without changing the boundary state.

The space groups #174, #187, #189, and #188, #190, where one cannot diagnose TI from SI, have the SI groups $\mathbb{Z}_3\times\mathbb{Z}_3$ and $\mathbb{Z}_3$, respectively, and the corresponding SI $z_{3m,0}$ and $z_{3m,\pi}$ are the mirror Chern numbers (mod 3) in the $k_3=0$ and $k_3=\pi$ planes. In #188 and #190 $z_{3m,\pi}$ is trivialized by nonsymmorphic symmetry and thus the corresponding SI groups reduce to $\mathbb{Z}_3$. In these space groups, the TI invariant is the parity of $C_{m,0}-C_{m,\pi}$[23] whereas SI have ambiguity for the parities of mirror Chern numbers; thus, TI can never be diagnosed from SI. For example, $z_{3m,0}=1$, $z_{3m,\pi}=0$ can correspond to $C_{m,0}=1$, $C_{m,\pi}=0$ (a TI), or $C_{m,0}=-2$, $C_{m,\pi}=0$ (not a TI).

Discussion

A byproduct of this study is a complete set of TCIs that can be layer-constructed in all 230 space groups (Supplementary Tables 5–8), even including groups not having SI. The abundance of the states thus obtained naturally suggests the question: are all TCI states exhausted in these layer constructions? We regret to answer it in the negative: LC cannot give us the weak topological insulator states in five space groups, namely #48, #86, #134, #201, and #224. In any one of the five, there is a weak indicator z_{2w}, but all layer-constructed states have $z_{2w}=0$. A common character of these space groups is that they have three perpendicular glide planes $\{m_{001}|\frac{1}{2}\frac{1}{2}0\}$ $\{m_{010}|\frac{1}{2}0\frac{1}{2}\}$ $\{m_{100}|0\frac{1}{2}\frac{1}{2}\}$ such that any single layer having weak index $z_{2w,i}=1$ would be doubled along the i-th direction and so the generated eLC has vanishing weak index. Explicit (non-LC) tight-binding models for the $z_{2w}=1$ states are given in Supplementary Note 6, completing the proof that for any non-zero SI there is at least one corresponding gapped topological state. These corner cases are somewhat surprising as weak TI have so far been considered most akin to stacking of decoupled 2D TI.

Finally, we comment that all LCs can be used to build 3D symmetry protected topological states of bosons and fermions protected by space group G plus a local group G_L. To do this one only needs to decorate each layer with a 2D SPT protected by G_L instead of the 2D TI.

Towards the completion of the work, we have been aware of a similar study[55]. To our knowledge, the results, when overlapping, are consistent with each other.

Methods

A short review of SIs. For each momentum in the Brillouin zone, there is an associate subgroup, called the little group, of the space group G, under the action of which the momentum is invariant up to a reciprocal lattice vector. A point is a high-symmetry point, denoted K_j, if its little group is greater than the little group of any point in the neighborhood. A fundamental theorem is that each band at momentum K_i or multiplet of degenerate bands corresponds to an irreducible representation of the little group at K_i. The symmetry data of a BS is defined as the an integer vector $\mathbf{n}$, each element of which, $n\left(\xi_i^{K_j}\right)$, is the number of appearance of the i-th irreducible representation in the valence bands at the j-th high-symmetry momentum K_j, where $i=1, ..., r_j$ labels the irreducible representations of the little group at K_j. One could further define the addition of two symmetry data as the addition of each entry, which corresponds to, physically, the superposition of two BSs.

For a gapped BS, the elements of its symmetry data cannot take arbitrary integers and there are constraints on the symmetry data known compatibility relations[40,41,43]. For example, gapped-ness requires that the occupation numbers at each K_i be the same, i.e., $\sum_i n\left(\xi_i^{K_j}\right)=$ const. All compatibility relations are linear equations so that the symmetry data satisfying all these relations again form a smaller linear space, termed the BS space, denoted {BS}.

On the other hand, we consider the symmetry data of AIs. In AIs, the bands are generated by decoupled atomic orbitals placed at certain Wyckoff positions in the unit cell. By this definition, one finds that the symmetry data of AIs also form a linear space, denoted {AI} (also called the space of band representations[41]). Obviously a symmetry data $\mathbf{n}\in$ {AI} satisfies all compatibility relations, so {AI} $\subseteq$ {BS}. One then naturally considers the quotient space $X_{BS}=$ {BS}/{AI}. X_{BS} is always a finite group generated by several $\mathbb{Z}_{n=2,3,4,6,8,12}$[40]. Each generator of X_{BS} is called an SI.

The following properties of indicators should be mentioned: any two gapped BSs having different sets of SI must be topologically distinct, and any two different symmetry data having the same set of SI only differ from each other by the symmetry data of an AI.

In ref. [40], the authors calculate the group structure of the indicators for all 230 space groups. However, it does not give explicit formulae for the generators. In order for application, we derive all these formulae in Supplementary Note 4.

Mirror Chern number of LC. Below we explicitly calculate the mirror Chern numbers of LC1 and LC2 in Fig. 2. As shown in Fig. 3e, in BZ of space group $P2/m$ there are two mirror-invariant planes, i.e., the $k_2 = 0$ and $k_2 = \pi$ planes; thus, we have two mirror Chern numbers $C_{m,0}$ and $C_{m,\pi}$. We assume there are only two occupied bands in the vertical 2D TCIs in LC2 and denote the corresponding Blöch wave functions as $|\phi_{\pm i}(\mathbf{k}_{2D}, x_2)\rangle$. Here, $\pm i$ represent the mirror eigenvalues, where i is the imaginary unit, $\mathbf{k}_{2D} = (k_1, k_3)$ is the 2D momentum, and x_2 is the position along $\mathbf{a}_2$ where the 2D TCIs are attached. We also assume that the wave functions with the mirror eigenvalue i $(-i)$ give a Chern number 1 (-1) such that the 2D mirror Chern number $C_m = 1$. Under the mirror operation $\hat{M}$ the 2D Blöch wave function $|\phi_{\pm i}(\mathbf{k}_{2D}, x_2)\rangle$ first get a mirror eigenvalue $\pm i$ and then move to the mirror position $-x_2$

$$\hat{M}|\phi_{\pm i}(\mathbf{k}_{2D}, x_2)\rangle = \pm i|\phi_{\pm i}(\mathbf{k}_{2D}, -x_2)\rangle \tag{3}$$

To calculate the mirror Chern numbers of LC2, we divide it into two subsystems: the eLC generated from A layer and the eLC generated from B layer (Fig. 3c). As the total mirror Chern numbers are the sum of mirror Chern numbers of the two subsystems, we need only to analyse the two subsystems, respectively. The 3D Blöch wave functions of A- and B-eLCs can be constructed as

$$|\psi^{A}_{\pm i}(\mathbf{k})\rangle = \sum_{x_2 = 0, \pm 1 \cdots} e^{ik_2 x_2}|\phi_{\pm i}(\mathbf{k}_{2D}, x_2)\rangle \tag{4}$$

$$|\psi^{B}_{\pm i}(\mathbf{k})\rangle = \sum_{x_2 = \pm\frac{1}{2}, \pm\frac{3}{2} \cdots} e^{ik_2 x_2}|\phi_{\pm i}(\mathbf{k}_{2D}, x_2)\rangle \tag{5}$$

Due to Eq. (3), it is direct to show that $|\psi^{A}_{i}(k_1, 0, k_3)\rangle$ and $|\psi^{A}_{i}(k_1, \pi, k_3)\rangle$, both of which are superpositions of $|\phi_i(\mathbf{k}_{2D}, x_2)\rangle$ and thus have the Chern number 1, have the same mirror eigenvalue i (Fig. 3d). Thus, for A-eLC m the mirror Chern numbers at $k_2 = 0$ and $k_2 = \pi$ are all 1. On the other hand, $|\psi^{B}_{i}(k_1, 0, k_3)\rangle$ and $|\psi^{B}_{i}(k_1, \pi, k_3)\rangle$, again both of which have the Chern number 1, have mirror eigenvalues i and $-i$, respectively (Fig. 3d). Thus, for B-eLC the mirror Chern numbers at $k_2 = 0$ and $k_2 = \pi$ are 1 and -1, respectively. Therefore, the total mirror Chern numbers in momentum space are $C_{m,0} = 2$ and $C_{m,\pi} = 0$ for LC2. It should be noticed that the values of $C_{m,0}$ and $C_{m,\pi}$ do not depend on the two band assumption we take: as long as the 2D TCI has $C_m = 1$, the results remain the same. On the other hand, the mirror Chern numbers of LC1 should be zero for both $k_2 = 0$ and $k_2 = \pi$ by the following argument. Without breaking mirror symmetry, each vertical plane can bend symmetrically towards the mirror plane until the two halves coincide on mirror-invariant planes in real space, due to the $\mathbb{Z}_2$-nature of each half, the folded plane is topologically equivalent to a trivial insulator. As LC1 can be smoothly trivialized without breaking mirror symmetry, it must have vanishing mirror Chern numbers.

Data availability

The data and code that support the findings of this study are available from the corresponding author upon reasonable request.

Received: 26 February 2018 Accepted: 30 July 2018
Published online: 30 August 2018

References

1. Thouless, D. J., Kohmoto, M., Nightingale, M. P. & den Nijs, M. Quantized hall conductance in a two-dimensional periodic potential. *Phys. Rev. Lett.* **49**, 405–408 (1982).
2. Haldane, F. D. M. Nonlinear field theory of large-spin heisenberg antiferromagnets: semiclassically quantized solitons of the one-dimensional easy-axis néel state. *Phys. Rev. Lett.* **50**, 1153–1156 (1983).
3. Affleck, I., Kennedy, T., Lieb, E. H. & Tasaki, H. Rigorous results on valence-bond ground states in antiferromagnets. *Phys. Rev. Lett.* **59**, 799–802 (1987).
4. Wen, X. G. Topological orders in rigid states. *Int. J. Mod. Phys. B* **04**, 239–271 (1990).
5. Kitaev, A. Y. Unpaired majorana fermions in quantum wires. *Phys.-Uspekhi* **44**, 131 (2001).
6. Kane, C. L. & Mele, E. J. Z_2. *Phys. Rev. Lett.* **95**, 146802 (2005).
7. Moore, J. E. & Balents, L. Topological invariants of time-reversal-invariant band structures. *Phys. Rev. B* **75**, 121306 (2007).
8. Fu, L., Kane, C. L. & Mele, E. J. Topological insulators in three dimensions. *Phys. Rev. Lett.* **98**, 106803 (2007).
9. Schnyder, A. P., Ryu, S., Furusaki, A. & Ludwig, A. W. W. Classification of topological insulators and superconductors in three spatial dimensions. *Phys. Rev. B* **78**, 195125 (2008).
10. Kitaev, A. Periodic table for topological insulators and superconductors. *AIP Conf. Proc.* **1134**, 22–30 (2009).
11. Gu, Z.-C. & Wen, X.-G. Tensor-entanglement-filtering renormalization approach and symmetry-protected topological order. *Phys. Rev. B* **80**, 155131 (2009).
12. Chen, X., Gu, Z.-C., Liu, Z.-X. & Wen, X.-G. Symmetry-protected topological orders in interacting bosonic systems. *Science* **338**, 1604–1606 (2012).
13. Lu, Y.-M. & Vishwanath, A. Theory and classification of interacting integer topological phases in two dimensions: a chern-simons approach. *Phys. Rev. B* **86**, 125119 (2012).
14. Bardeen, W. A. Anomalous ward identities in spinor field theories. *Phys. Rev.* **184**, 1848–1859 (1969).
15. Haldane, F. D. M. Model for a quantum hall effect without landau levels: Condensed-matter realization of the "parity anomaly". *Phys. Rev. Lett.* **61**, 2015–2018 (1988).
16. Ryu, S., Moore, J. E. & Ludwig, A. W. W. Electromagnetic and gravitational responses and anomalies in topological insulators and superconductors. *Phys. Rev. B* **85**, 045104 (2012).
17. Bernevig, B. A., Hughes, T. L. & Zhang, S.-C. Quantum spin hall effect and topological phase transition in hgte quantum wells. *Science* **314**, 1757–1761 (2006).
18. Chang, C.-Z. et al. Experimental observation of the quantum anomalous hall effect in a magnetic topological insulator. *Science* **340**, 167–170 (2013).
19. Liu, J. et al. Spin-filtered edge states with an electrically tunable gap in a two-dimensional topological crystalline insulator. *Nat. Mater.* **13**, 178–183 (2013).
20. Qian, X., Liu, J., Fu, L. & Li, J. Quantum spin hall effect in two-dimensional transition metal dichalcogenides. *Science* **346**, 1344–1347 (2014).
21. Fang, C. & Fu, L. Rotation anomaly and topological crystalline insulators. Preprint at https://arxiv.org/abs/1709.01929 (2017).
22. Zhang, H. et al. Topological insulators in bi2se3, bi2te3 and sb2te3 with a single dirac cone on the surface. *Nat. Phys.* **5**, 438–442 (2009).
23. Hsieh, T. H. et al. Topological crystalline insulators in the snte material class. *Nat. Commun.* **3**, 982 (2012).
24. Wang, Z., Alexandradinata, A., Cava, R. J., & Bernevig, B. A. Hourglass fermions. *Nature* **532**, 189–194 (2016).
25. Wieder, B. J. et al. Wallpaper fermions and the topological dirac insulator. Preprint at https://arxiv.org/abs/1705.01617 (2017).
26. König, M. et al. Quantum spin hall insulator state in hgte quantum wells. *Science* **318**, 766–770 (2007).
27. Chen, Y. L. et al. Experimental realization of a three-dimensional topological insulator, bi2te3. *Science* **325**, 178–181 (2009).
28. Hsieh, D. et al. A tunable topological insulator in the spin helical dirac transport regime. *Nature* **460**, 1101–1105 (2009).
29. Tanaka, Y. et al. Experimental realization of a topological crystalline insulator in snte. *Nat. Phys.* **8**, 800–803 (2012).
30. Dziawa, P. et al. Topological crystalline insulator states inpb1?xsnxse. *Nat. Mater.* **11**, 1023–1027 (2012).
31. Xu, S.-Y. et al. Observation of a topological crystalline insulator phase and topological phase transition in pb(1−x)Sn(x)Te. *Nat. Commun.* **3**, 1192 (2012).
32. Ma, J. et al. Experimental evidence of hourglass fermion in the candidate nonsymmorphic topological insulator khgsb. *Sci. Adv.* **3**, e1602415 (2017).
33. Hahn, T. *International Tables for Crystallography*. (International Union of Crystallography by Kluwer Academic Publishers, Dordrecht, London, 2002).
34. Bradley, C. J. & Cracknell, A. P. *The Mathematical Theory of Symmetry in Solids: Representation Theory for Point Groups and Space Groups* (Oxford Univ. Press, 2010).
35. Fu, L. & Kane, C. L. Topological insulators with inversion symmetry. *Phys. Rev. B* **76**, 045302 (2007).
36. Turner, A. M., Zhang, Y. & Vishwanath, A. Entanglement and inversion symmetry in topological insulators. *Phys. Rev. B* **82**, 241102 (2010).
37. Hughes, T. L., Prodan, E. & Bernevig, B. A. Inversion-symmetric topological insulators. *Phys. Rev. B* **83**, 245132 (2011).
38. Fang, C., Gilbert, M. J. & Bernevig, B. A. Bulk topological invariants in noninteracting point group symmetric insulators. *Phys. Rev. B* **86**, 115112 (2012).
39. Fu, L. Topological crystalline insulators. *Phys. Rev. Lett.* **106**, 106802 (2011).
40. Po, H. C., Vishwanath, A. & Watanabe, H. Symmetry-based indicators of band topology in the 230 space groups. *Nat. Commun.* **8**, 50 (2017).
41. Bradlyn, B. et al. Topological quantum chemistry. *Nature* **547**, 298–305 (2017).
42. Bradlyn, B. et al. Band connectivity for topological quantum chemistry: band structures as a graph theory problem. *Phys. Rev. B* **97**, 035138 (2018).

43. Kruthoff, J., de Boer, J., van Wezel, J., Kane, C. L. & Slager, R.-J. Topological classification of crystalline insulators through band structure combinatorics. *Phys. Rev. X* **7**, 041069 (2017).
44. Altland, A. & Zirnbauer, M. R. Nonstandard symmetry classes in mesoscopic normal-superconducting hybrid structures. *Phys. Rev. B* **55**, 1142–1161 (1997).
45. Teo, J. C. Y., Fu, L. & Kane, C. L. Surface states and topological invariants in three-dimensional topological insulators: application to $bi_{1-x}sb_x$. *Phys. Rev. B* **78**, 045426 (2008).
46. Shiozaki, K. & Sato, M. Topology of crystalline insulators and superconductors. *Phys. Rev. B* **90**, 165114 (2014).
47. Song, Z., Fang, Z. & Fang, C. $(d-2)$-dimensional edge states of rotation symmetry protected topological states. *Phys. Rev. Lett.* **119**, 246402 (2017).
48. Kresse, G. & Hafner, J. Ab initio. *Phys. Rev. B* **48**, 13115–13118 (1993).
49. Kresse, G. & Furthmüller, J. Efficiency of ab-initio total energy calculations for metals and semiconductors using a plane-wave basis set. *Comput. Mater. Sci.* **6**, 15–50 (1996).
50. Isobe, H. & Fu, L. Theory of interacting topological crystalline insulators. *Phys. Rev. B* **92**, 081304 (2015).
51. Fulga, I. C., Avraham, N., Beidenkopf, H. & Stern, A. Coupled-layer description of topological crystalline insulators. *Phys. Rev. B* **94**, 125405 (2016).
52. Ezawa, M. Hourglass fermion surface states in stacked topological insulators with nonsymmorphic symmetry. *Phys. Rev. B* **94**, 155148 (2016).
53. Song, H., Huang, S.-J., Fu, L. & Hermele, M. Topological phases protected by point group symmetry. *Phys. Rev. X* **7**, 011020 (2017).
54. Huang, S.-J., Song, H., Huang, Y.-P. & Hermele, M. Building crystalline topological phases from lower-dimensional states. *Phys. Rev. B* **96**, 205106 (2017).
55. Khalaf, E., Po, H. C., Vishwanath, A. & Watanabe, H. Symmetry indicators and anomalous surface states of topological crystalline insulators. Preprint at https://arxiv.org/abs/1711.11589 (2017).

Acknowledgements

We acknowledge support from Ministry of Science and Technology of China under grant numbers 2016YFA0302400 and 2016YFA0300600, National Science Foundation of China under grant number 11674370 and 11421092, and from Chinese Academy of Sciences under grant number XXH13506-202.

Author contributions

C.F. conceived the work and devised the main method to obtain the main results. Z.D.S. did the major part of the calculations. C.F. and Z.F. wrote the main text, whereas Z.D.S. and T.T.Z. wrote the Supplementary Information and plot all figures and tables.Data availabilityThe data and code that support the findings of this study are available from the corresponding author upon reasonable request.

Additional information

Supplementary Information accompanies this paper at https://doi.org/10.1038/s41467-018-06010-w.

Competing interests: The authors declare no competing interests.

Reprints and permission information is available online at http://npg.nature.com/reprintsandpermissions/

Publisher's note: Springer Nature remains neutral with regard to jurisdictional claims in published maps and institutional affiliations.

ARTICLE

https://doi.org/10.1038/s41586-019-0944-6

Catalogue of topological electronic materials

Tiantian Zhang[1,2,9], Yi Jiang[1,2,9], Zhida Song[1,2,9], He Huang[3], Yuqing He[2,3], Zhong Fang[1,4], Hongming Weng[1,5,6,7,8]* & Chen Fang[1,4,6,7,8]*

Topological electronic materials such as bismuth selenide, tantalum arsenide and sodium bismuthide show unconventional linear response in the bulk, as well as anomalous gapless states at their boundaries. They are of both fundamental and applied interest, with the potential for use in high-performance electronics and quantum computing. But their detection has so far been hindered by the difficulty of calculating topological invariant properties (or topological nodes), which requires both experience with materials and expertise with advanced theoretical tools. Here we introduce an effective, efficient and fully automated algorithm that diagnoses the nontrivial band topology in a large fraction of nonmagnetic materials. Our algorithm is based on recently developed exhaustive mappings between the symmetry representations of occupied bands and topological invariants. We sweep through a total of 39,519 materials available in a crystal database, and find that as many as 8,056 of them are topologically nontrivial. All results are available and searchable in a database with an interactive user interface.

Symmetry and topology in solids are an entangled pair of concepts in modern physics. Since 2005, theorists[1–3] have been aware that, in the presence of time-reversal symmetry, there are insulators (or nondegenerate ground states with a finite excitation gap in general) that deviate drastically from atomic insulators. These new special insulators host nontrivial topology in their electronic band structures, quantified by a new, global good quantum number—the Z_2 invariant[4,5]. This invariant takes the value of either 0 or 1, and depends on the wavefunctions of the valence bands in the entire Brillouin zone.

Topological insulators, protected by time-reversal symmetry with the Z_2 invariant, were only the first member of an entire family of topological materials to come in the following decade. It is now understood that topological invariants are the defining properties of all topological materials and that they can take different forms, which depend, and depend only, on the dimensionality and the symmetries of the system[6–8]. These symmetries range from on-site symmetries such as time reversal and particle–hole interchange, to spatial symmetries such as translation[3], reflection[9], rotation[10–12] and nonsymmorphic symmetries[13,14], each of which brings new and independent topological invariants. Hence a full characterization of the topology of a given crystal amounts to listing all of the invariants protected by all elements in the corresponding space group.

Parallel to this line of investigation has been the emergence of the field of topological semimetals[15–20], in which the conduction and the valence bands have band crossings—that is, topological nodes that cannot be removed by symmetry-preserving perturbations. Depending on the degeneracy and dimensionality of their nodes, topological semimetals can be further classified into nodal-point and nodal-line semimetals. A topological semimetal is characterized by the number and the type of all of its band crossings[21].

Numerical prediction of topological materials thus requires the evaluation of all topological invariants, or the identification of all topological nodes, both of which amount to involved calculations[22]. The expressions of some topological invariants are highly complicated[13,23,24] for direct evaluation, and some invariants do not even have close-form expressions[10–12]. The challenge has prevented people from carrying out any large-scale, comprehensive search for topological materials, and successful examples have been ascribed mostly to the experience and intuition of researchers.

Following the theory of topological quantum chemistry[25] and that of symmetry-based indicators[26], a series of recent theoretical works has greatly improved the situation by completely mapping the irreducible representations of valence bands onto topological invariants[27–29] and topological nodes[30]. Recognizing that these theories can be fused together with first-principles numerical methods, we have developed a fully automated search algorithm that can readily be used to scan through large materials databases.

Algorithm

We now briefly describe the automatic diagnostic process that we have designed for any given nonmagnetic crystal (Fig. 1). Some important technical details needed to reproduce our findings are given in the Methods.

In the preparation phase, we import a material that is simultaneously registered in the online crystal database the Materials Project (https://materialsproject.org)[31] and the Inorganic Crystal Structure Database (ICSD; http://www2.fiz-karlsruhe.de/icsd_home.html)[32]. If the material has a magnetic moment higher than 0.1 μ_B per unit cell (according to its Materials Project record), we label it as 'magnetic' and stop further analysis, as the theory works for nonmagnetic materials only. Also excluded from further analysis are materials with an odd number of electrons per unit cell, which are labelled as 'conventional metals'. Otherwise, we proceed to standardize the input crystal structure for the next phase.

In the calculation phase, the imported atomic positions and a certain set of pseudopotentials are first used to obtain the self-consistent electron density using the Vienna ab initio simulation package (VASP)[33].

[1]Beijing National Laboratory for Condensed Matter Physics and Institute of Physics, Chinese Academy of Sciences, Beijing, China. [2]University of Chinese Academy of Sciences, Beijing, China. [3]Computer Network Information Center, Chinese Academy of Sciences, Beijing, China. [4]Kavli Institute for Theoretical Sciences, Chinese Academy of Sciences, Beijing, China. [5]Collaborative Innovation Center of Quantum Matter, Beijing, China. [6]Songshan Lake Materials Laboratory, Dongguan, China. [7]CAS Centre for Excellence in Topological Quantum Computation, Beijing, China. [8]Physical Science Laboratory, Huairou National Comprehensive Science Center, Beijing, China. [9]These authors contributed equally: Tiantian Zhang, Yi Jiang, Zhida Song. *e-mail: hmweng@iphy.ac.cn; cfang@iphy.ac.cn

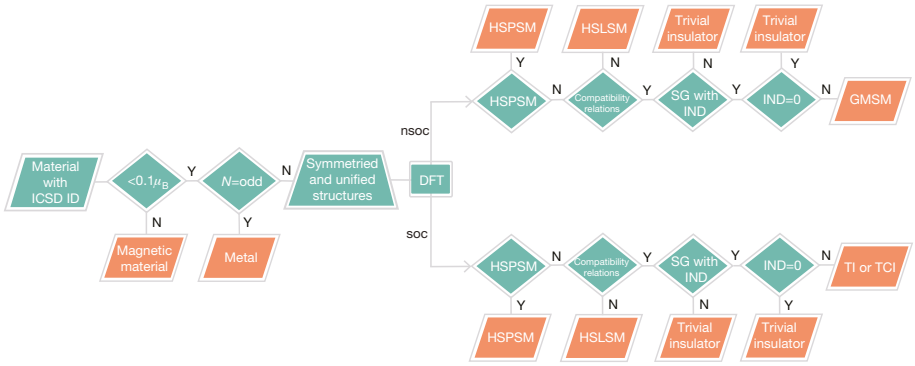

Fig. 1 | Flow chart for our automatic diagnostic algorithm. For a given material found in the ICSD and the Materials Project, we first check against the record at the Materials Project to see whether it is nonmagnetic (that is, does it have a magnetic moment less than 0.1 μ_B per unit cell), and whether there is an even number of electrons in one primitive unit cell. If yes for both, we feed the material into a density-functional-theory (DFT) calculation of the band structure and compute symmetry data, before checking whether there are partially filled irreducible representations at high-symmetry points. If not, the symmetry data are checked against all compatibility relations, and, should all relations be satisfied, the data are fed into the calculation of symmetry-based indicators. At each checkpoint, a material either goes on to the next step, or is labelled as magnetic, conventional metal, high-symmetry point semimetal or high-symmetry line semimetal. At the final step, depending on the values of indicators, a material is labelled as GMSM, TI, TCI or insulator with trivial indicators. At the first-principles calculation step and all following steps, two possible settings are applied to all steps: nsoc or soc. DFT, density functional theory; IND, symmetry-based indicator(s); SG, space group.

Once the density converges, it is used to compute the energy levels and wavefunctions at a given list of high-symmetry points in the Brillouin zone. At each high-symmetry point, we rank the energy levels from low to high, and we define the first N bands as the valence bands (Fig. 2), where N is the number of electrons per unit cell. (Note that this working definition deviates from the conventional notion of valence bands.) We store the wavefunctions of all occupied bands at high-symmetry points for the next phase.

In the analysis phase, using a script in conjunction with the data on the Bilbao Crystallographic Server[34], we identify the irreducible representation for each (multiplet of) valence band(s). Then, from this, another script is used to check whether there is band touching or crossing between the Nth and the N+1-th band at any high-symmetry point or along any high-symmetry line, the latter of which requires an exhaustive list of compatibility relations, also available on the Bilbao Crystallographic Server thanks to recent efforts[25,34]. A material that has degeneracy at high-symmetry points or high-symmetry lines is labelled as high-symmetry-point semimetal (HSPSM) or high-symmetry-line semimetal (HSLSM), respectively. For a band structure that does not have such degeneracy, we proceed to compute all of its symmetry-based indicators. Symmetry-based indicators[26] directly inform whether the material is a topological insulator, a topological crystalline insulator (TCI) or a topological semimetal, and give all possible sets of the topological invariants[27,28] or topological nodes[30]. From the values of the indicators, the material can be labelled as generic-momenta semimetal (GMSM, having topological nodes at non-high-symmetry momenta), topological insulator or TCI. This concludes the final phase of the algorithm.

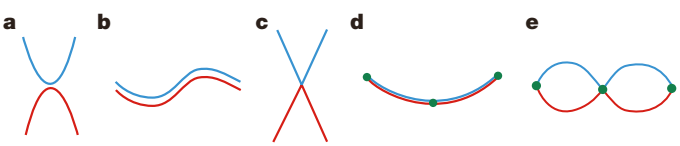

Fig. 2 | Definition of valence bands and conduction bands. The red band represents the top valence and the blue the bottom conduction band, for the following cases: **a**, insulator or semiconductor; **b**, compensation semimetal; **c**, topological semimetal; **d**, metal with an odd number of electrons per unit cell on a centrosymmetric lattice; and **e**, metal with an odd number of electrons per unit cell on a noncentrosymmetric lattice. The green dots in **d**, **e** represent Kramer's degeneracy owing to time-reversal symmetry. Note that our definitions for **d**, **e** differ from conventional definitions.

Identification of five topological classes

We have run the above algorithm through a total of 39,519 crystals, of which we find 10,348 to be magnetic, and 2,483 to be conventional metals. We carried out first-principles calculations for 26,522 materials, from which we detect 8,056 topological materials in the presence of spin–orbit coupling, sorted into 2,713 HSPSMs, 2,292 HSLSMs, 1,814 topological insulators and 1,237 TCIs.

In electronic systems, the spin–orbit coupling is always finite, but there are materials consisting of light atoms that have negligible spin–orbit coupling—that is, the spin–orbit coupling is much smaller compared with other energy scales such as the Fermi energy or temperature. For these materials, diagnosing the topology while assuming an absence of spin–orbit coupling is physically more relevant. For example, identifying graphene as a Dirac semimetal is more relevant than declaring it to be a topological insulator with a gap of roughly 10^{-6} eV. Because of this, for each material, we carry out the calculation and analysis twice—once with spin–orbit coupling ('soc setting') and once without ('nsoc setting'). When using the nsoc setting, materials that have band degeneracy between the valence and conduction bands at high-symmetry points and along high-symmetry lines are also sorted as HSPSM and HSLSM, respectively. If the band structure does not have any such degeneracy, we proceed to calculate the symmetry-based indicators. In the absence of spin–orbit coupling, all indicators correspond to topological nodes at non-high-symmetry momenta[30], and therefore materials that have non-zero indicators are all GMSMs. The type and configuration of the topological nodes for each non-zero set of indicators are found in ref. [30]. For the nsoc setting, we find 8,889 materials to be topological, classified as 5,508 HSPSMs, 3,269 HSLSMs and 112 GMSMs.

Each material is now labelled with one of the following: HSPSM, high-symmetry point semimetal (both settings); HSLSM, high-symmetry line semimetal (both settings); GMSM, generic-momenta semimetal (nsoc setting only); TI, topological insulator (soc setting only); TCI, topological crystalline insulator (soc setting only); magnetic; conventional metal; or insulator with trivial indicators. Out of these, we consider the first five classes to be topological materials; we list the materials according to their class in Supplementary Tables I–V. In Supplementary Table I, each HSPSM material is shown together with high-symmetry points at which partial fillings occur, and irreducible representations that are partially filled. Each HSLSM material in Supplementary Table II is shown together with the high-symmetry line(s) at which band crossings between the Nth and the N+1-th bands appear. Each GMSM, TI and TCI material—listed in Supplementary Tables III, IV and V respectively—is shown together with the values of its symmetry-based indicators.

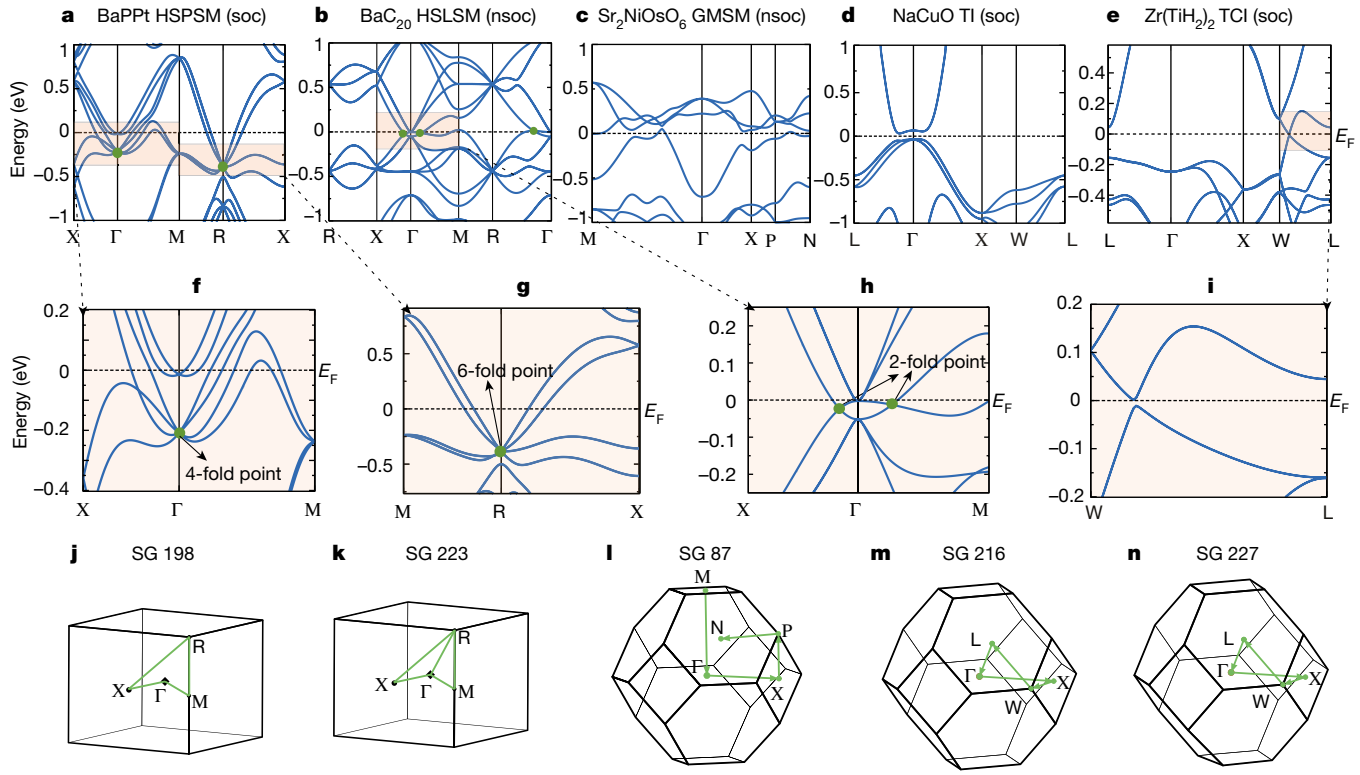

Fig. 3 | The five candidates for the five classes of topological material. **a**, **f**, **g**, **j**, The HSPSM BaPPt, which has sixfold degeneracy near the Fermi energy at R. **b**, **h**, **k**, The HSLSM BaC_{20}, which has negligible spin–orbit coupling and nine connected nodal rings centred at Γ. **c**, **l**, The GMSM Sr_2NiOsO_6, with nodal rings that have Z_2-monopole charge (nsoc setting). **d**, **m**, The topological insulator NaCuO. **e**, **i**, **n**, The TCI $Zr(TiH_2)_2$. For each candidate material, we plot the band structure in **a**–**e**, the Brillouin zone with high-symmetry points in **j**–**n**, and if necessary, zoomed-in regions of the band structure **f**–**i**.

Our extensive sweep of materials includes a large fraction of all crystals ever synthesized, and we detect nontrivial topology in about 30% of the 26,522 calculated nonmagnetic materials. This abundance of topological materials overturns the sentiment of many, including us, that they are special and rare in nature. Without any tuning parameter or human intervention, these many materials from the sweep include almost all topological materials known so far, such as bismuth selenide (Bi_2Se_3), a topological insulator; tin telluride (SnTe), a TCI; and sodium bismuthide (Na_3Bi), a topological semimetal. More importantly, this catalogue includes materials for which the nontrivial topology was previously unknown.

Representative materials from the five topological classes

Below we choose one candidate from each class for discussion. Out of the five, four have not, to the best of our knowledge, been discussed previously in the literature, and four host new topological invariants or topological nodes that have not been experimentally discovered in real materials. We find barium phosphorus platinum (BaPPt; Fig. 3a)[35,36] to be a HSPSM, in which the conduction and the valence bands meet at the high-symmetry points Γ and R. The degeneracy at R is sixfold-stabilized by nonsymmorphic space-group symmetries, and importantly there is an electron pocket near R. These facts qualify BaPPt (soc setting) as a good candidate for the study of topological nodes beyond Weyl and Dirac nodes in real materials[37].

From the HSLSM class, we highlight cubic barium fullerene (BaC_{20}; Fig. 3b; nsoc setting), from space group 223; this material has one fullerene and three barium atoms per unit cell. The violation of compatibility relations along Γ–X, Γ–M and Γ–R indicates band crossings along these three lines and their symmetry partners. Further analysis (see Methods) shows that these crossing points are parts of the nine interconnected nodal rings that are centred at Γ.

The osmium double perovskite Sr_2NiOsO_6 (Fig. 3c; nsoc setting), a GMSM, does not have any band crossings along any of the high-symmetry lines, but the symmetry indicators of (0002) imply that at generic momenta there must be 2-mod-4 nodal rings where the conduction and the valence bands cross. Each of the rings has Z_2-topological charge[38], making Sr_2NiOsO_6 the first candidate electronic material (with small spin–orbit coupling) that hosts Z_2-nontrivial nodal rings.

Sodium oxocuprate (NaCuO; soc setting) is a new noncentrosymmetric topological insulator (Fig. 3d), having three band inversions between the *d*-orbital and the *s*-orbital at Γ, with an inverted bandgap of about 0.1 eV. For noncentrosymmetric systems, the classical Fu–Kane formula[39] does not apply, so an eigenvalue diagnosis would be impossible without our new method.

Finally, zirconium titanium hydride ($Zr(TiH_2)_2$; Fig. 3e) has band crossings along L–W without spin–orbit coupling, but as the coupling turns on it opens a full gap of about 10 meV at all momenta, making the material a TCI. The symmetry indicators of (0002) pin down the topological invariants of this TCI to two possible sets. Our method cannot distinguish them further, but a calculation of the mirror Chern number at the $k_z = 0$ plane helps us to choose the correct set (see Methods). In this set, all non-zero invariants are protected by screw-rotation symmetries or glide-plane symmetries, so that $Zr(TiH_2)_2$ is a materials candidate for a screw-axis Z_2 TCI, having one-dimensional helical edge states on its surface without two-dimensional surface states for certain sample configurations (see Methods for details). Such TCIs are also known as second-order topological insulators[40–42].

The entire catalogue is available at http://materiae.iphy.ac.cn/, which has an interactive user interface that facilitates searching of the vast amount of data. It also shows the band structures and density of states for each material diagnosed as topological.

Discussion

Although the abundance of topological materials in nature is good news, the immediate difficulty is that we do not have a simple way

of ranking these many candidates, because there is no universal standard for an ideal topological material. Sometimes it is one that has a topological bandgap or topological Fermi surface that does not coexist with trivial pockets of carriers; but sometimes we particularly look for the presence and interplay of the latter (for example in the case of the recently discovered topological superconductivity in iron selenide, FeSe[43–45]). Some people are interested in three-dimensional topological states[46]; but quasi-two-dimensional topological materials are also desirable for good reasons[47]. Some want the coexistence of band topology and ferroelectricity[48], and some are looking for a high receptibility to magnetic or superconducting dopants[49]. We have adopted a relatively traditional standard in the field of topological materials: that better topological gapped materials have larger energy gaps (for topological insulators and TCIs), and better topological gapless materials have a lower density of states (for HSPSMs, HSLSMs and GMSMs), with the caveat that the criterion of low density of states does not apply to nodal-line semimetals in general. For each material in the catalogue, we have computed the density of states versus energy, from which we have extracted the energy gap (if any) and the density of states at the Fermi energy. On the basis of these two pieces of data, we have ranked the materials from each class for every space group, using || to separate materials that are better by this standard from the rest (see Supplementary Information). We emphasize that our ranking should only be considered as a reference, and we suggest that readers interested in a particular candidate material should eye-inspect the band structure shown in our online database.

The main outcome of our work is the sorting of nonmagnetic materials into topological classes; we did not aim to find the 'best' topological materials. However, it is natural to ask how we would compare the materials found in this exhaustive, sweeping search with those found previously in an ad hoc fashion. We note that, as almost all previously known topological materials have already been included in the catalogue, we can only compare the known materials with the new members in each class. A simple comparison reveals that the newly found materials are not substantially better than the known ones, as judged by our standard of a large gap or smaller density of states. The previously known bismuth selenide (Bi_2Se_3) is still the best candidate for a topological insulator in the catalogue, having a gap of around 0.31 eV—larger than the roughly 0.16-eV gap in the best new candidate, strontium lead telluride (Sr_2Te_4Pb). The most studied TCI is SnTe, with a gap of 0.188 eV, larger than the 0.072-eV gap of the new candidate Yb_3PbO (an ytterbium perovskite). The best HSLSM in the literature is probably Na_3Bi, with space group 194; among the newly discovered materials, the best such material is probably indium antimonide (InSb), with space group 186. The two materials both have Dirac points along Γ–A and a vanishing density of states.

Our method has demonstrated its power in showing the abundance of nontrivial topology that nature has to offer. However, it is equally, if not more, important to expound on the limitations of the method, and to offer caveats to users of the catalogue, which we summarize as follows.

First, the entire theoretical framework of our diagnosis is based on the assumption that valence electrons can be characterized by the physical picture of band theory. However, this assumption breaks down in the presence of strong electron correlation. For this reason, we cannot hope to include any strongly interacting symmetry-protected topological states[50] that have been theoretically proposed, such as the Haldane chain[51].

Second, we have used first-principles simulations to calculate band structures without any corrections ascribed to electron correlation, for the latter require additional artificial parameters. For this reason, band structures of materials consisting of *d*- and *f*-electrons[52,53] near the Fermi energy may be incorrect. Thus, in Supplementary Tables I–V, certain elements that are known to host partially filled *d*- or *f*-electrons in compounds are marked with blue or red, respectively. Users should be aware that the first-principles calculation has a tendency to overestimate the inverted bandgap.

Third, our method—or indeed any eigenvalue diagnosis method—takes as inputs only those symmetry data that are found at certain high-symmetry points, and therefore cannot detect band inversions away from these points. This is the origin of the one-to-many nature of the mappings from symmetry-based indicators to topological invariants[27,28] or nodes[30]. Physically, it means that if some nontrivial topology derives from band inversions away from any high-symmetry point, the diagnosis would not detect it, instead identifying the material as trivial. This leads to the absence of the famous Weyl semimetal tantalum arsenide (TaAs) from the catalogue. TaAs[54,55] has band inversions at Σ and S, neither of which is a high-symmetry point.

Fourth, our method assumes the nonmagnetic state of a material when diagnosing topology, but cannot diagnose magnetism itself. The magnetic moment listed on the Materials Project website has been calculated using a first-principles simulation with an additional parameter, Hubbard U, and a ferromagnetic initial state. This simple numerical diagnosis is not supposed to capture any type of antiferromagnetism, and may also misidentify some ferromagnetism as nonmagnetism (and vice versa). We suggest that readers interested in a particular material should check for possible magnetism in the experimental literature.

Fifth, in some materials—such as bismuth bromide (Bi_4Br_4) and lithium silver antimide (Li_2AgSb)—the ordering of bands near the Fermi energy depends critically on the lattice constants or the choice of pseudopotential. As a rule, we have used the experimental lattice parameters without relaxation. But if the gap in a material is very small, we would suggest doing the calculation again with slightly different input parameters (such as relaxed lattice constants) to see whether the result is stable.

Finally, conventional metals can in principle also be called HSPSMs, because at each of the eight time-reversal invariant momenta, the *N*th and the *N*+1-th bands necessarily touch owing to Kramer's degeneracy. However, these materials usually have trivial carrier pockets that are far larger than the topological ones, and we therefore exclude them from our list of topological materials.

Conclusion

We have designed an algorithm for quickly diagnosing nontrivial topology in nonmagnetic materials, using only the symmetry data from high-symmetry points in the Brillouin zone as inputs. We have applied the algorithm to all materials registered in the Materials Project and the ICSD. Contrary to popular thinking that nontrivial topology is exotic and scarce, we have found that more than 30% (8,056 out of 26,688) of the studied materials are topological.

Online content

Any methods, additional references, Nature Research reporting summaries, source data, statements of data availability and associated accession codes are available at https://doi.org/10.1038/s41586-019-0944-6.

Received: 5 July 2018; Accepted: 19 December 2018;
Published online 27 February 2019.

1. Kane, C. L. & Mele, E. J. Z. Z_2 topological order and the quantum spin Hall effect. *Phys. Rev. Lett.* **95**, 146802 (2005).
2. Bernevig, B. A., Hughes, T. L. & Zhang, S. C. Quantum spin Hall effect and topological phase transition in HgTe quantum wells. *Science* **314**, 1757–1761 (2006).
3. Fu, L., Kane, C. L. & Mele, E. J. Topological insulators in three dimensions. *Phys. Rev. Lett.* **98**, 106803 (2007).
4. Hasan, M. Z. & Kane, C. L. Colloquium: topological insulators. *Rev. Mod. Phys.* **82**, 3045 (2010).
5. Qi, X. L. & Zhang, S. C. Topological insulators and superconductors. *Rev. Mod. Phys.* **83**, 1057 (2011).
6. Schnyder, A. P., Ryu, S., Furusaki, A. & Ludwig, A. W. Classification of topological insulators and superconductors in three spatial dimensions. *Phys. Rev. B* **78**, 195125 (2008).
7. Kitaev, A. Periodic table for topological insulators and superconductors. *AIP Conf. Proc.* **1134**, 22–30 (2009).
8. Chiu, C. K., Teo, J. C., Schnyder, A. P. & Ryu, S. Classification of topological quantum matter with symmetries. *Rev. Mod. Phys.* **88**, 035005 (2016).
9. Hsieh, T. H. et al. Topological crystalline insulators in the SnTe material class. *Nat. Commun.* **3**, 982 (2012); corrigendum 4, 1901 (2013).

10. Song, Z., Fang, Z. & Fang, C. (*d*-2)-dimensional edge states of rotation symmetry protected topological states. *Phys. Rev. Lett.* **119**, 246402 (2017).
11. Fang, C. & Fu, L. Rotation anomaly and topological crystalline insulators. Preprint at https://arxiv.org/abs/1709.01929 (2017).
12. Schindler, F. et al. Higher-order topological insulators. *Sci. Adv.* **4**, eaat0346 (2018).
13. Wang, Z., Alexandradinata, A., Cava, R. J. & Bernevig, B. A. Hourglass fermions. *Nature* **532**, 189–194 (2016).
14. Wieder, B. J. et al. Wallpaper fermions and the nonsymmorphic Dirac insulator. *Science* **361**, 246–251 (2018).
15. Fang, Z. et al. The anomalous Hall effect and magnetic monopoles in momentum space. *Science* **302**, 92–95 (2003).
16. Murakami, S. Phase transition between the quantum spin Hall and insulator phases in 3D: emergence of a topological gapless phase. *New J. Phys.* **9**, 356 (2007); corrigendum **10**, 029802 (2008).
17. Wan, X., Turner, A. M., Vishwanath, A. & Savrasov, S. Y. Topological semimetal and Fermi-arc surface states in the electronic structure of pyrochlore iridates. *Phys. Rev. B* **83**, 205101 (2011).
18. Young, S. M. et al. Dirac semimetal in three dimensions. *Phys. Rev. Lett.* **108**, 140405 (2012).
19. Wang, Z. et al. Dirac semimetal and topological phase transitions in A_3Bi (A= Na, K, Rb). *Phys. Rev. B* **85**, 195320 (2012).
20. Burkov, A. A., Hook, M. D. & Balents, L. Topological nodal semimetals. *Phys. Rev. B* **84**, 235126 (2011).
21. Armitage, N. P., Mele, E. J. & Vishwanath, A. Weyl and Dirac semimetals in three-dimensional solids. *Rev. Mod. Phys.* **90**, 015001 (2018).
22. Yu, R., Qi, X. L., Bernevig, A., Fang, Z. & Dai, X. Equivalent expression of Z_2 topological invariant for band insulators using the non-abelian Berry connection. *Phys. Rev. B* **84**, 075119 (2011).
23. Fang, C. & Fu, L. New classes of three-dimensional topological crystalline insulators: nonsymmorphic and magnetic. *Phys. Rev. B* **91**, 161105 (2015).
24. Shiozaki, K., Sato, M. & Gomi, K. Z. Z_2 topology in nonsymmorphic crystalline insulators: Möbius twist in surface states. *Phys. Rev. B* **91**, 155120 (2015).
25. Bradlyn, B. et al. Topological quantum chemistry. *Nature* **547**, 298–305 (2017).
26. Po, H. C., Vishwanath, A. & Watanabe, H. Symmetry-based indicators of band topology in the 230 space groups. *Nat. Commun.* **8**, 50 (2017); erratum **8**, 931 (2017).
27. Song, Z., Zhang, T., Fang, Z. & Fang, C. Quantitative mappings between symmetry and topology in solids. *Nat. Commun.* **9**, 3530 (2018).
28. Khalaf, E., Po, H. C., Vishwanath, A. & Watanabe, H. Symmetry indicators and anomalous surface states of topological crystalline insulators. *Phys. Rev. X* **8**, 031070 (2018).
29. Kruthoff, J., de Boer, J., van Wezel, J., Kane, C. L. & Slager, R. J. Topological classification of crystalline insulators through band structure combinatorics. *Phys. Rev. X* **7**, 041069 (2017).
30. Song, Z., Zhang, T. & Fang, C. Diagnosis for nonmagnetic topological semimetals in the absence of spin-orbital coupling. *Phys. Rev. X* **8**, 031069 (2018).
31. Jain, A. et al. Commentary: the materials project: a materials genome approach to accelerating materials innovation. *APL Mater.* **1**, 011002 (2013).
32. Hellenbrandt, M. The inorganic crystal structure database (ICSD)—present and future. *Crystallogr. Rev.* **10**, 17–22 (2004).
33. Kresse, G. & Furthmüller, J. Efficient iterative schemes for ab initio total-energy calculations using a plane-wave basis set. *Phys. Rev. B* **54**, 11169 (1996).
34. Elcoro, L. et al. Double crystallographic groups and their representations on the Bilbao Crystallographic Server. *J. Appl. Cryst.* **50**, 1457–1477 (2017).
35. Chang, G. et al. Unconventional chiral fermions and large topological Fermi arcs in RhSi. *Phys. Rev. Lett.* **119**, 206401 (2017).
36. Flicker, F. et al. Chiral optical response of multifold fermions. *Phys. Rev. B* **98**, 155145 (2018).
37. Bradlyn, B. et al. Beyond Dirac and Weyl fermions: unconventional quasiparticles in conventional crystals. *Science* **353**, aaf5037 (2016).
38. Fang, C., Chen, Y., Kee, H. Y. & Fu, L. Topological nodal line semimetals with and without spin-orbital coupling. *Phys. Rev. B* **92**, 081201 (2015).
39. Fu, L. & Kane, C. L. Topological insulators with inversion symmetry. *Phys. Rev. B* **76**, 045302 (2007).
40. Benalcazar, W. A., Bernevig, B. A. & Hughes, T. L. Quantized electric multipole insulators. *Science* **357**, 61–66 (2017).
41. Langbehn, J., Peng, Y., Trifunovic, L., von Oppen, F. & Brouwer, P. W. Reflection-symmetric second-order topological insulators and superconductors. *Phys. Rev. Lett.* **119**, 246401 (2017).
42. Benalcazar, W. A., Bernevig, B. A. & Hughes, T. L. Electric multipole moments, topological multipole moment pumping, and chiral hinge states in crystalline insulators. *Phys. Rev. B* **96**, 245115 (2017).
43. Zhang, P. et al. Observation of topological superconductivity on the surface of an iron-based superconductor. *Science* **360**, 182–186 (2018).
44. Wang, D. et al. Evidence for Majorana bound states in an iron-based superconductor. *Science* **362**, 333–335 (2018).
45. Yin, J. X. et al. Observation of a robust zero-energy bound state in iron-based superconductor Fe (Te, Se). *Nat. Phys.* **11**, 543–546 (2015).
46. Zhang, H. et al. Topological insulators in Bi_2Se_3, Bi_2Te_3 and Sb_2Te_3 with a single Dirac cone on the surface. *Nat. Phys.* **5**, 438–442 (2009).
47. Qian, X., Liu, J., Fu, L. & Li, J. Quantum spin Hall effect in two-dimensional transition metal dichalcogenides. *Science* **346**, 1344–1347 (2014).
48. Chang, K. et al. Discovery of robust in-plane ferroelectricity in atomic-thick SnTe. *Science* **353**, 274–278 (2016).
49. Chang, C. Z. et al. Experimental observation of the quantum anomalous Hall effect in a magnetic topological insulator. *Science* **340**, 167–170 (2013).
50. Gu, Z. C. & Wen, X. G. Tensor-entanglement-filtering renormalization approach and symmetry-protected topological order. *Phys. Rev. B* **80**, 155131 (2009).
51. Affleck, I. Quantum spin chains and the Haldane gap. *J. Phys. Condens. Matter* **1**, 3047 (1989).
52. Dzero, M., Sun, K., Galitski, V. & Coleman, P. Topological kondo insulators. *Phys. Rev. Lett.* **104**, 106408 (2010).
53. Lu, F., Zhao, J., Weng, H., Fang, Z. & Dai, X. Correlated topological insulators with mixed valence. *Phys. Rev. Lett.* **110**, 096401 (2013).
54. Weng, H., Fang, C., Fang, Z., Bernevig, B. A. & Dai, X. Weyl semimetal phase in noncentrosymmetric transition-metal monophosphides. *Phys. Rev. X* **5**, 011029 (2015).
55. Huang, S. M. et al. A Weyl Fermion semimetal with surface Fermi arcs in the transition metal monopnictide TaAs class. *Nat. Commun.* **6**, 7373 (2015).

Acknowledgements We are grateful for suggestions and comments from M. Liu, B. Bradlyn, H. Watanabe and B. Wieder. We acknowledge support from the Ministry of Science and Technology of China under grant numbers 2016YFA0302400, 2016YFA0300600 and 2018YFA0305700; the National Science Foundation of China under grant numbers 11674370, 11421092 and 11674369; and the Chinese Academy of Sciences under grant numbers XXH13506-202, XDB07020100 and XDB28000000. We also acknowledge support from the Science Challenge Project (number TZ2016004), the K. C. Wong Education Foundation (GJTD-2018-01), the Beijing Municipal Science and Technology Commission (Z181100004218001) and the Beijing Natural Science Foundation (Z180008).

Reviewer information *Nature* thanks J. Checkelsky, M. Franz and the other anonymous reviewer(s) for their contribution to the peer review of this work.

Author contributions C.F. conceived the work; H.W. and Z.F. were in charge of the numerical methods and checked for consistency with previous works; T.Z. did the major part of the calculations and analyses of materials; Y.J., Z.S., H.H. and Y.H. wrote the code for analysing irreducible representations and symmetry-based indicators; H.H. and Y.H. built the website. C.F., H.W. and Z.F. wrote the main text; and T.Z., Y.J. and Z.S wrote the Methods section and the Supplementary Information.

Competing interests The authors declare no competing interests.

Additional information
Extended data is available for this paper at https://doi.org/10.1038/s41586-019-0944-6.
Supplementary information is available for this paper at https://doi.org/10.1038/s41586-019-0944-6.
Reprints and permissions information is available at http://www.nature.com/reprints.
Correspondence and requests for materials should be addressed to H.W. or C.F.
Publisher's note: Springer Nature remains neutral with regard to jurisdictional claims in published maps and institutional affiliations.

METHODS

Choice of input crystal data. Crystal data—including space-group numbers, lattice parameters (a, b, c, α, β, γ) and atomic positions—are imported from the experimental values recorded in the Materials Project[31,56]. To the best of our knowledge, the Materials Project collects experimental crystal data from the ICSD[32] and reorganizes them. The ICSD has duplicated entries; to handle this, the Materials Project identifies two materials as the same if their lattice parameters and atomic positions differ by values less than a given threshold. The Materials Project also has a requirement for the accuracy of atomic positions, so that if the position of any atom cannot be experimentally determined up to a preset error, the corresponding material would not be added to the Materials Project. Taking into account duplicates and data accuracy, the 199,466 records in ICSD become 39,519 records in the Materials Project.

The Materials Project is a database of materials with their properties obtained from standardized numerical simulations. One of the properties is magnetism, which is given in terms of the total magnetic moment per unit cell, in units of μ_B. This value is obtained from a density functional theory (DFT) calculation or a DFT + U calculation, with a ferromagnetic initial state of the electrons. We comment that a more reliable way of determining potential magnetism is to use various possible magnetic structures in the initial state, and to compare the convergent energies, identifying the lowest energy state as the ground state. However, it is unclear how one could reasonably enumerate all candidate magnetic structures, so the diagnosis for magnetism is generally considered difficult. We note that for several materials, the calculated magnetic moment differs from experimental data. For example, $MnAlCo_2$ and Fe_5Si_3 have been found to be ferromagnetic at lower temperatures, yet they show negligible magnetic moments in their Materials Project records. We note that antiferromagnetism is not thought to be captured by the numerical simulations either.

Band topology is mostly stable against small perturbations in the lattice parameters. Yet there are certain materials for which the gaps are so close to the inversion point that a small change in lattice parameters leads to a transition from nontopological to topological and vice versa. For example, for Ca_3NBi and $TlBiSe_2$, results of the topological diagnosis depend on whether the experimental value or the calculated value of the lattice constants is used. Here, the calculated value refers to the value after a simulated relaxation of the lattice, optimizing the total energy.

In addition, before feeding the crystal data to the DFT calculation, we check the consistency between the atomic positions and the space group. We find 166 materials that do not pass the consistency test within an error of up to 0.1 Å, and exclude them from further processing.

Band topology in conventional metals. Materials that have an odd number of electrons per unit cell are labelled as conventional metals and excluded from further diagnosis. The reason is simple: all these materials should be classified as HSPSMs, so analysis becomes unnecessary. This is because all bands are at least doubly degenerate at time-reversal momenta owing to Kramer's degeneracy. Any odd number filling then necessarily leads to partial filling at every time-reversal momentum, making the material a HSPSM.

We note that further classification among these metals, which we do not perform here, amounts to determining the dimension of the band crossing. For example, if there is inversion symmetry, then time reversal and inversion jointly protect double degeneracy at every momentum in the Brillouin zone: this is three-dimensional crossing. In the presence of a twofold screw axis, this symmetry together with time reversal lead to double degeneracy at an entire high-symmetry plane, which is a two-dimensional crossing at the boundary of the Brillouin zone. In the presence of a glide plane, this symmetry together with time reversal lead to double degeneracy along certain lines at the boundary of the Brillouin zone, and this crossing is one dimensional. If none of screw axis, glide plane or inversion is present, the bands are generally nondegenerate at any momentum away from a time-reversal invariant momentum, so that these momenta are discrete Weyl points—that is, zero-dimensional crossings.

Settings for the first-principles calculation. All of the calculations herein are performed by VASP[33,57–59] with the generalized gradient approximation (GGA) of the Perdew–Burke–Ernzerhof (PBE)-type exchange-correlation potential. The pseudopotential files that we used are from the VASP software package and are listed at http://materiae.iphy.ac.cn/. The cut-off energy of the plane wave basis set is set to be the ENMAX value in the pseudopotential file plus 25%. A Γ-centred Monkhorst–Pack grid with 30 k-points per $Å^{-1}$ is used for the self-consistent calculations. A maximum number of electronic self-consistency steps is given in our calculations, such that a material for which the calculation does not converge within 300 self-consistency loop steps is labelled and discarded. Two itinerant schemes are used in this process: the special Davidson block iteration scheme, and residual minimization method direct inversion in the iterative subspace (RMM-DIIS). About 400 materials are not converged or converge to wrong states in the nsoc setting, and 600 in the soc-setting.

While the mapping from symmetry data to topology data is mathematically rigorous, the validity of GGA depends on the actual material: if a material has a significant correlation effect at the Fermi energy, the results are likely to be inaccurate. For example, for compounds containing rare-earth elements with possibly partial-filling f-orbitals, the strong correlation effect is dominant; we have left these materials for further detailed study. From experience, in Supplementary Tables I–V we have highlighted a few elements that often induce strong correlation effects in compounds owing to partially filled d- or f-shells (blue for d and red for f). We have not highlighted titanium, yttrium, zirconium, niobium, molybdenum, lanthanum, lutetium, hafnium, tantalum, tungsten and platinum because, although they have partially filled d-shells, in many known cases they do not bring about strong correlation effects.

The original data loaded from the Materials Project are not in a unified convention; for example, the orientation of the primitive cell is arbitrary, as is the choice of origin point. In order to implement automated high-throughput calculations and to ensure that VASP can find the right symmetry, we symmetrize and standardize the atomic positions using PHONOPY[60] after loading the lattice parameters and atomic positions. At this step, we discarded 166 materials for discrepancy in the space groups identified in PHONOPY and those given in the databases, up to an error tolerance of 0.1 Å in atomic position.

Extracting irreducible representations. The irreducible representation for each group of degenerate valence bands is obtained by calculating the character of each symmetry operation and looking up the character tables on the Bilbao Crystallographic Server. To be specific, first the plane wave expansion coefficients of wavefunctions are read from the VASP output file, and then, by applying different space-group symmetry operations to the wavefunctions, we obtain the corresponding character. Attention needs to be paid in the choice of convention in symmetry operations, including the coordinate origin and orientation, as well as the spin rotation axis of the SU(2) part of the symmetry operation. In determining the presence of degeneracy, we use an energy error of min(0.5 meV, 0.1 $\Delta_{\boldsymbol{k}}$, where $\Delta_{\boldsymbol{k}}$ is the gap between valence bands and conduction bands at the $\boldsymbol{k}$-point) to avoid possible numerical level splitting from VASP. Failing to find irreducible representations formed by 'degenerate' bands identified in this way implies a low quality of convergence. In such cases we improve the convergence threshold and redo the self-consistent and non-self-consistent calculations until we can successfully identify each group of degenerate bands with a certain irreducible representation.

Nodal lines in BaC_{20}. Using the nsoc setting, we identify BaC_{20} (space group 223) as an HSLSM, the band structure of which breaks compatibility relations along Γ–X, Γ–M and Γ–R. Below we show that these crossings are intersections of nine nodal rings with high symmetry lines in the Brillouin zone, wherein three of the rings lie in the $\boldsymbol{k}_i = 0 (i = x, y, z)$ planes and six lie in the $\boldsymbol{k}_i \pm \boldsymbol{k}_j = 0 (i, j = x, y, z, i \neq j)$ planes. The $\boldsymbol{k}_i = 0$ rings can be diagnosed from the crossings along Γ–X and Γ–M, both of which interchange a valence band having a mirror ($\{m_{001}|0\}$) eigenvalue of -1 with a conduction band with a mirror eigenvalue of $+1$. Because of these crossings, the valence bands at Γ have one more (or less) -1 (or $+1$) mirror eigenvalue than the valence bands at X or M, implying nodal ring(s) protected by the mirror symmetry in the $\boldsymbol{k}_z = 0$ plane. Such mirror eigenvalues at Γ, X and M allow a few possible configurations of the ring(s). For example, there may be a single ring surrounding Γ; or there may be a single ring surrounding X, a single ring surrounding Y (that is, the C_3 ($\{3_{111}|000\}$) partner of X in the $\boldsymbol{k}_y$ axis) and a single ring surrounding M; and so on. Further band-structure calculation shows that BaC_{20} belongs to the first case, that is, it has a single ring surrounding Γ in the $\boldsymbol{k}_z = 0$ plane. Owing to the C_3 rotation symmetry, there are in total three nodal rings in the $\boldsymbol{k}_i = 0$ planes (Extended Data Fig. 1a). The $\boldsymbol{k}_i \pm \boldsymbol{k}_j = 0$ rings can be diagnosed in a similar way: the crossings along the Γ–M and Γ–R interchange a valence band having a glide ($\{m_{1\bar{1}0}|\frac{1}{2}\frac{1}{2}\frac{1}{2}\}$) eigenvalue $e^{-i\boldsymbol{t}\cdot\boldsymbol{k}/2}$ with a conduction band having a glide eigenvalue $-e^{-i\boldsymbol{t}\cdot\boldsymbol{k}/2}$, where $\boldsymbol{t} = \left(\frac{1}{2}\frac{1}{2}\frac{1}{2}\right)$. It follows that valence bands at Γ have one more (less) $e^{-i\boldsymbol{t}\cdot\boldsymbol{k}/2}$ ($-e^{-i\boldsymbol{t}\cdot\boldsymbol{k}/2}$) glide eigenvalue than the valence bands at M or R. On the other hand, the band structure along R–X, and along R–Z, where Z is the C_3 partner of X in the $\boldsymbol{k}_z$ axis, preserves all the compatibility relations; thus Z has the same glide eigenvalues with R and M. Therefore, similar to the case for the $\boldsymbol{k}_z = 0$ plane, the glide eigenvalues allow a few possible configurations for the ring(s) in the $\boldsymbol{k}_x - \boldsymbol{k}_y = 0$ plane. For example, there may be a single ring surrounding Γ, or there may be a single ring surrounding M, a single ring surrounding R, and a single ring surrounding Z, and so on. Further band-structure calculation certifies the first case—that is, there is a single ring surrounding Γ in the $\boldsymbol{k}_x - \boldsymbol{k}_y = 0$ plane. Then, owing to the space-group symmetries, there are in total six nodal rings in the $\boldsymbol{k}_i \pm \boldsymbol{k}_j = 0 (i \neq j)$ planes (Extended Data Fig. 1b). Numerical calculations show that the rings in the $\boldsymbol{k}_i \pm \boldsymbol{k}_j = 0 (i \neq j)$ planes have a larger radius than the rings in the $\boldsymbol{k}_i = 0$ planes.

Topological invariants of $Zr(TiH_2)_2$. In order to determine the topological invariants of $Zr(TiH_2)_2$ (space group 227) with the soc setting, we look up its symmetry-indicator set—which is $(Z_{2w-1}; Z_{2w-2}; Z_{2w-3}; Z_4) = (0002)$ —in Extended Data

Table 1 and find that there are only two possibilities for the invariants for this symmetry-indicator set. In the first case, the mirror Chern number on the $\bar{1}10$ plane in the Brillouin zone (the yellow plane in Extended Data Fig. 2a) is 2 (mod 4), whereas in the second case this mirror Chern number is 0 (mod 4). By ab initio calculation, as described in the next paragraph, we find that this mirror Chern number is 0 and thus $Zr(TiH_2)_2$ belongs to the second case. In this case, nontrivial TCI invariants include: (i) an hourglass invariant protected by glide symmetry $\{m_{001}|\frac{1}{4}\frac{1}{4}0\}$; (ii) a rotation invariant protected by $\{2_{1\bar{1}0}|000\}$; (iii) an inversion invariant; (iv) a screw invariant protected by $\{4_{001}|0\frac{1}{4}\frac{1}{4}\}$; and those invariants protected by symmetries equivalent with above symmetries. All of these invariants are Z_2-type and correspond to either two-dimensional or one-dimensional anomalous surface states.

Here we propose two real space configurations to detect such surface states. In Extended Data Fig. 2c, we show the one-dimensional helical modes protected by screws and/or inversion. The cubic sample is cut out along the (100), (010) and (001) surfaces, all of which are fully gapped. As long as the cube preserves inversion symmetry, there must be an inversion-symmetric one-dimensional helical mode on the boundary, whose shape depends on the experimental situation. However, in presence of the fourfold screw symmetries, which protect nontrivial screw invariants, the shape of helical mode is further constrained. We consider the sample to be large enough such that the fourfold screw symmetry, $\{4_{001}|0\frac{1}{4}\frac{1}{4}\}$, is preserved on the side surfaces far away from the top and bottom surfaces. Then, as discussed in refs [9,10], four one-dimensional helical modes run along the screw axis and transform to each other in turn under the screw operation. Similarly, along any equivalent screw axis there also exist four one-dimensional helical modes. The helical mode shown in Extended Data Fig. 2c is a configuration satisfying all of the above symmetry conditions. In Extended Data Fig. 2d, we show the two-dimensional surface states protected by glide and/or twofold rotation symmetries. The sample is cut out along (110), $(1\bar{1}0)$ and (001) surfaces, wherein the (001) surface is fully gapped whereas the (110) and $(1\bar{1}0)$ surfaces are gapless. Owing to the hourglass invariant being protected by $\{m_{001}|\frac{1}{4}\frac{1}{4}0\}$, the $(1\bar{1}0)$ surface must have an hourglass mode, and owing to the rotation invariant being protected by $\{2_{1\bar{1}0}|000\}$, the $(1\bar{1}0)$ surface must have 2 (mod 4) Dirac nodes. In fact, the two kinds of surface states are consistent with each other: at an even filling number, which is necessary for an insulator in the presence of time-reversal symmetry, the two hourglass crossings protected by glide symmetry also play the role of Dirac nodes for the rotation invariant. Therefore the $(1\bar{1}0)$ surface has a C_2-symmetric hourglass mode. The (110) surface has a similar surface state because it is equivalent with the $(1\bar{1}0)$ surface.

Now let us briefly describe how we calculate the mirror Chern number. First, the parallelogram spanned by $\boldsymbol{G_1}$ and $\boldsymbol{G_2}$ (Extended Data Fig. 2a) is recognized as the minimal periodic cell in the mirror plane, wherein $\boldsymbol{G_1}$ is along the (110) direction and $\boldsymbol{G_2}$ is along the (111) direction ($\boldsymbol{G_1}$ and $\boldsymbol{G_2}$ are reciprocal lattice basis vectors). We therefore calculate the mirror Chern number within this parallelogram. For each point along the Γ $\boldsymbol{G_1}$ line, $\boldsymbol{kG_1}$, we define a Wilson-loop matrix as:

$$W_{n,n'}(\boldsymbol{k}) = \sum_{n_1 n_2 \cdots n_{N-1} \in \mathrm{occ}} u_{n,\boldsymbol{kG_1}} | u_{n_1,\boldsymbol{kG_1}+\frac{1}{N}\boldsymbol{G_2}} u_{n_1,\boldsymbol{kG_1}+\frac{1}{N}\boldsymbol{G_2}} | u_{n_2,\boldsymbol{kG_1}+\frac{2}{N}\boldsymbol{G_2}}$$
$$\times u_{n_{N-2},\boldsymbol{kG_1}+\frac{N-2}{N}\boldsymbol{G_2}} | u_{n_{N-1},\boldsymbol{kG_1}+\frac{N-1}{N}\boldsymbol{G_2}} u_{n_{N-1},\boldsymbol{kG_1}+\frac{N-1}{N}\boldsymbol{G_2}} | \hat{V}^{\boldsymbol{G_2}} | u_{n',\boldsymbol{kG_1}}$$

where N is a large enough integer to describe the infinite limit; $|u_{n,k}\rangle$ is the periodic part of the Bloch wavefunction; n, n', n_i are the valence-band indices; and $\hat{V}^{\boldsymbol{G_2}}$ is the embedding operator[61]. For each $\boldsymbol{kG_1}$ we can define the mirror representation matrix as:

$$M_{n,n'}(\boldsymbol{k}) = u_{n,\boldsymbol{kG_1}} \mid \hat{M} \mid u_{n',\boldsymbol{kG_1}}$$

where $\hat{M}$ is the operator of symmetry operation $\{m_{1\bar{1}0}|0\}$. One can prove that $M(\boldsymbol{k})$ always commutes with $W(\boldsymbol{k})$. Therefore, we can project the Wilson-loop matrix into the subspace having mirror eigenvalue $+i$; the mirror Chern number is then given simply by the winding number of the projected Wilson loop. In Extended Data Fig. 2b, we plot the eigenvalues of the projected Wilson-loop matrix as a function of $\boldsymbol{k}$, from which one can find that the winding number is 0.

Ranking candidate materials. We rank the candidates in each class of topological materials with each space group by their density of states at the Fermi energy, from low to high, in Supplementary Tables I–V. For materials having zero density of states, we rank them by the size of the energy gap, from large to small. The density of states is obtained from a non-self-consistent calculation by using a Γ-centred Monkhorst–Pack grid with 40 k-points per $Å^{-1}$, the tetrahedron method for Brillouin zone integrations, and a number of 5,000 grid points in energy from E_f −4 eV to +4 eV (where E_f is the Fermi energy for a material). The gap is extracted from the density-of-states profile, by finding the gap between the tails of the conduction and the valence bands. To be specific, we first find the highest unoccupied energy levels in presence of $\pm 10^{-3}$ additional electrons per unit cell, and then calculate the gap as the difference of these two levels. The momentum grid that we use for the self-consistent calculation is not large enough to extract an accurate density of states at the Fermi energy, nor is it sufficient to resolve fine features in the density of states as a function of energy. The standard of zero density of states at the Fermi energy applies well to finding good topological insulators and topological crystalline insulators. However, for topological semimetals, this simple standard is not very reliable. Nodal-point semimetals—such as Weyl and Dirac semimetals—should ideally have a Fermi surface that shrinks to discrete points, and the density of states near the Fermi energy should scale as $\sim(E-E_f)^2$. Therefore, it is the functional behaviour, rather than the absolute values, of the density of states that distinguish these semimetal states. Our calculation, as stated above, does not have sufficiently large momentum sampling to reliably extract such functional behaviours. For nodal-line semimetals, the standard is even more irrelevant, as the density of states of ideal nodal-line semimetals should be linearly dependent on the length of the nodal line, which is unknown a priori. We comment that the calculated density of states, and the ranking therein, should only be used as a reference in selecting candidates from the classes of HSPSM, HSLSM and GMSM for further research.

Topology beyond eigenvalue diagnosis. Our method, based on the theoretical tools developed in refs [25–28,30], is an eigenvalue diagnostic scheme, first introduced in refs [25,26]. In ref. [26], it is proved that all of the symmetry eigenvalues at high-symmetry points in a band structure can be mapped to a certain element in a finite group called the symmetry-based indicators. The group structures of indicators are derived in ref. [26], and their explicit expressions in refs [27,28,30]. The indicators for each space group, if they exist, are a set of several Z_n numbers, and they (roughly speaking) quantify how any given symmetry data differ from those of an atomic insulator with the same crystal structure.

The symmetry indicators have the following properties: first, if any indicator is non-zero, the material is not an atomic insulator, that is, it is topologically nontrivial; second, two materials with different indicators are topologically distinct; and third, the topological distinction between two materials that have the same indicators cannot be diagnosed using symmetry data. We note that the third point means that all information on topology that may be extracted from symmetry data has been contained in the values of indicators. One should be aware that the third point implies that there are different topologies that cannot be distinguished using indicators. This is most easily seen in the example of mirror Chern numbers: ref. [28] proves that if two systems have the same indicators, they may differ in the mirror Chern number by $2n$, where n is the order of rotation symmetry in the system. In fact, refs [27,28] show that mapping from indicators to invariants is one-to-many in general: one given set of indicators maps to several inequivalent sets of topological invariants. Physically, this is because the band inversions can in principle happen away from any high-symmetry point; and given that band inversions may change the topology, there can be two topologically distinct band structures that have identical eigenvalues at all high-symmetry points, rendering powerless any eigenvalue diagnostic scheme. For the same reason, the materials that have zero indicators are not necessarily topologically trivial: we can only say that their topology, if any, is undetectable using our method or any eigenvalue diagnosis.

Data availability

All results are available and searchable with an interactive user interface at http://materiae.iphy.ac.cn. Codes for obtaining the irreducible representations are available from the corresponding author upon reasonable request.

56. Ong, S. P. et al. Python Materials Genomics (pymatgen): a robust, open-source python library for materials analysis. *Comput. Mater. Sci.* **68**, 314–319 (2013).
57. Kresse, G. & Hafner, J. *Ab initio* molecular-dynamics simulation of the liquid-metal–amorphous-semiconductor transition in germanium. *Phys. Rev. B* **49**, 14251 (1994).
58. Kresse, G. & Furthmüller, J. Efficiency of ab-initio total energy calculations for metals and semiconductors using a plane-wave basis set. *Comput. Mater. Sci.* **6**, 15–50 (1996).
59. Kresse, G. & Hafner, J. Ab initio molecular dynamics for liquid metals. *Phys. Rev. B* **47**, 558 (1993).
60. Togo, A. & Tanaka, I. First principles phonon calculations in materials science. *Scr. Mater.* **108**, 1 (2015).
61. Alexandradinata, A., Wang, Z. & Bernevig, B. A. Topological Insulators from Group Cohomology. *Phys. Rev. X* **6**, 021008 (2016).

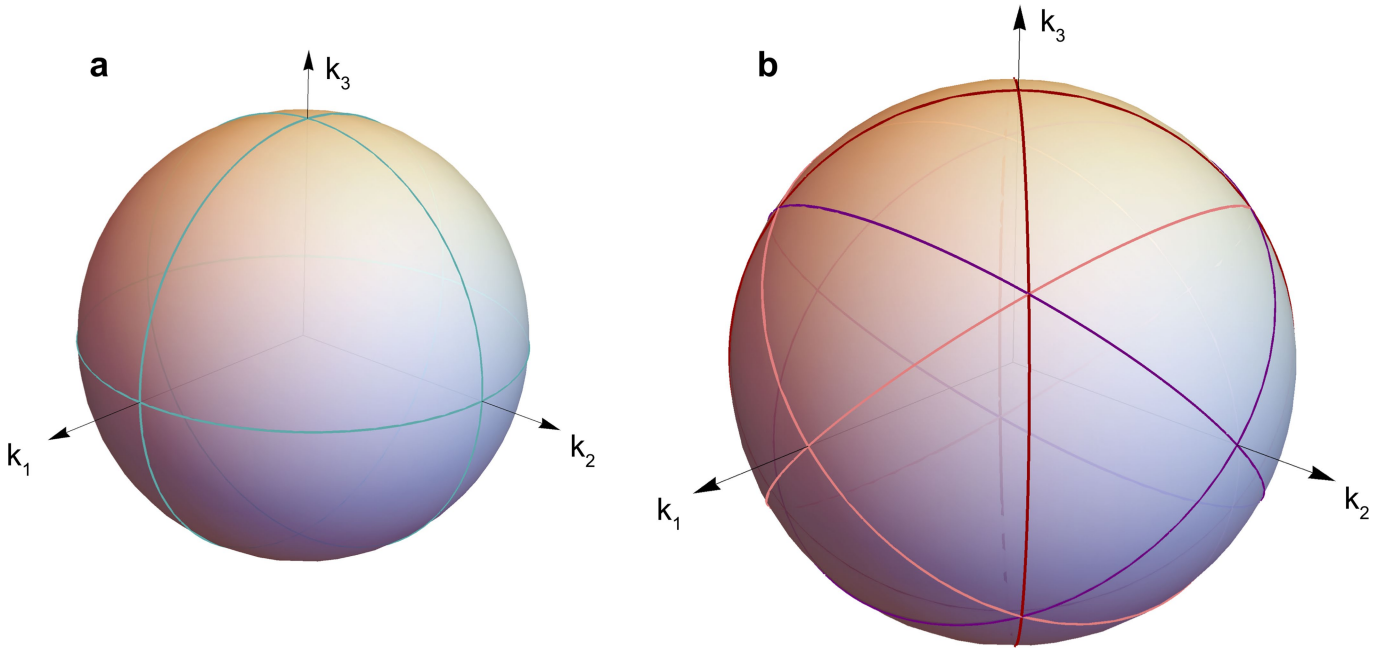

Extended Data Fig. 1 | Nodal-ring configuration in BaC_{20} (nsoc setting). This material is in space group Pm$\bar{3}$n. **a**, The three equivalent nodal rings in the $\boldsymbol{k}_i = 0 (i = x, y, z)$ planes, protected by the mirror symmetries on these planes. **b**, The six equivalent nodal rings in the $\boldsymbol{k}_i \pm \boldsymbol{k}_j = 0 (i, j = x, y, z,\ \ i \neq j)$ planes, protected by the glide symmetries on these planes.

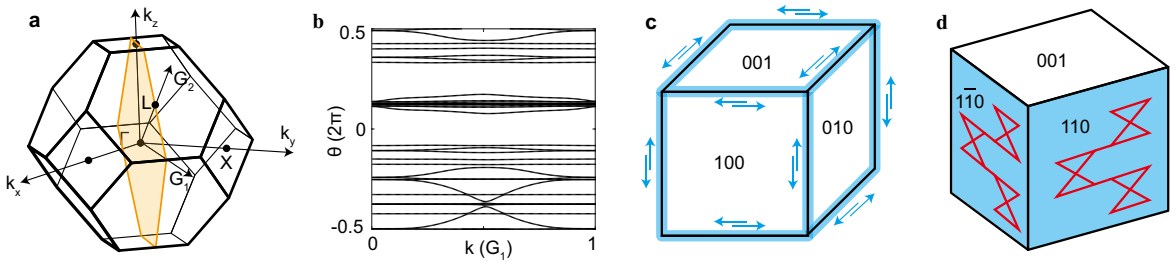

Extended Data Fig. 2 | Topological invariants and surface states of $Zr(TiH_2)_2$. **a**, Brillouin zone for $Zr(TiH_2)_2$, in which the yellow plane is $m_{1\bar{1}0}$. **b**, Wilson loop for $Zr(TiH_2)_2$ in the $m_{1\bar{1}0}$ plane. **c**, One-dimensional helical modes in a cubic $Zr(TiH_2)_2$ sample. **d**, Two-dimensional surface states on each surface of a cubic $Zr(TiH_2)_2$ sample.

Extended Data Table 1 | Possible invariants for space group 227

$Z_{2,2,2,4}$	weak	$m_{(2)}^{010}$	$g_{\frac{1}{4}\frac{1}{4}0}^{001}$	$g_{\frac{1}{4}4^{-}0}^{001}$	$g_{\frac{1}{4}\frac{1}{4}\frac{1}{4}}^{101}$	2^{001}	2^{011}	i	2_1^{001}	2_1^{011}	4_1^{001}	4_3^{001}	$\bar{4}^{001}$
0000	000	0	0	0	0	0	0	0	0	0	0	0	0
0000	000	2	0	0	**1**	0	**1**	0	0	**1**	**1**	**1**	**1**
0002	000	0	**1**	**1**	0	0	**1**	**1**	0	**1**	**1**	**1**	0
0002	000	2	**1**	**1**	**1**	0	0	**1**	0	0	0	0	**1**

$Z_{2,2,2,4}$ are the four symmetry-based indicators. The remainder of the labels in the top row refer to topological invariants protected by various lattice symmetries as defined in ref. [27], in which: 'weak' denotes weak topological indices; $m_{(2)}^{010}$ shows the mirror Chern number which takes a value between -1 and $+2$, protected by the (010)-mirror plane; $\boldsymbol{G}_{abc}^{mnl}$ denotes the Z_2 invariant protected by a glide plane perpendicular to the *mnl* direction with glide vector *abc*; *i* is the Z_2 invariant protected by inversion symmetry about the origin; and $n_{\boldsymbol{k}}^{mnl}$ is the Z_2 invariant protected by an *n*-fold rotation about the *mnl* direction followed by a translation along the same direction through the $\boldsymbol{k}/n$ lattice vector.